Tectono-Thermal History of the Neoarchean Balehonnur Shear Zone, Western Dharwar Craton (Southern India)

B. Tarun Kumar, M. Jayananda, P. Nasipuri, Martin Guitreau, K. Aadhiseshan, S. Rao, T. Tarun Thomas, M. Satyanarayanan

GeoScienceWorld
Lithosphere
Volume 2022, Article ID 4167477, 21 pages
https://doi.org/10.2113/2022/4167477

Lithosphere

Research Article

Tectono-Thermal History of the Neoarchean Balehonnur Shear Zone, Western Dharwar Craton (Southern India)

B. Tarun Kumar,[1] M. Jayananda,[1] P. Nasipuri,[2] Martin Guitreau,[3] K. R. Aadhiseshan,[1] S. V. Balaji Manasa Rao,[1] T. Tarun Thomas,[1] and M. Satyanarayanan[4]

[1]*Centre for Earth, Ocean & Atmospheric Sciences, University of Hyderabad, Hyderabad 500 046, India*
[2]*Department of Earth and Environmental Sciences, IISER Bhopal, Bhopal, India*
[3]*Laboratoire Magmas et Volcans, Observatoire de Physique du Globe de Clermont-Ferrand, Universite Clermont Auvergne, IRD, CNRS, UMR 6524, 6 Avenue Blaise Pascal, 63178 Aubière, France*
[4]*CSIR-National Geophysical Research Institute, Uppal Road, Hyderabad 500 007, India*

Correspondence should be addressed to M. Jayananda; jayanandam@uohyd.ac.in

Received 2 March 2022; Revised 12 August 2022; Accepted 22 September 2022; Published 25 October 2022

Academic Editor: Eugene Grosch

A widely spaced Neoarchean shear zone network traverses the granite-greenstone terrains of the Western Dharwar craton (WDC). The NNW-SSE trending Balehonnur shear zone traverses the largest part of the preserved tilted Archean crustal ensemble in the Western Dharwar craton (WDC) from the amphibolite-granulite transition in the south to greenschist facies in the north and eventually concealed under Deccan lava flows. Published tectonic fabrics data and kinematic analysis, with our data reveal a sinistral sense of shearing that effectuate greenstone sequences, Tonalite-Trondhjemite-Granodiorite Gneisses (TTG), and Koppa granite as reflected in variable deformation and strain localization. A profound increase of strain towards the core of the shear zone in the ca. 2610 Ma Koppa granite is marked by a transition from weak foliation outside the shear zone through the development of C-S structures and C-prime fabrics, mylonite to ultramylonite. The mineral assemblages in the Koppa granite and adjoining greenstone indicate near peak *P-T* conditions of 1.2 Gpa, 775-800°C following a slow cooling path of 1.0 GPa and 650°C. Field-based tectonic fabrics data together with U-Pb zircon ages reveal that the Koppa granite emplaced along the contact zone of Shimoga-Bababudan basin ca. 2610 Ma, coinciding with the emplacement of ca. 2600 Ma Arsikere-Banavara, Pandavpura, and Chitradurga granites further east which mark the stabilization of WDC. Significant variation in major element oxide (SiO_2 = 56-69 wt.%) together with high content of incompatible elements (REE, Nb, Zr, and Y) and high zircon crystallization temperatures (~1000°C) of Koppa granite suggests derivation by partial melting of composite sources involving enriched uppermost mantle and lower crust. The development of widely spaced shear zones is probably linked to the assembly of eastern and western blocks through westward convergence of hot oceanic lithosphere against already cratonized thick colder western block leading to the development of strain heterogeneities between greenstone and TTGs due to their different mineral assemblages leading to rheological contrast in the cratonic lithologies.

1. Introduction

In recent years, understanding the tectonic strain of Precambrian terrains has been a subject of renewed interest [1, 2]. The Pilbara (Western Australia), Kaapvaal craton (Southern Africa), and Western Dharwar craton (Southern India) preserve dome and keel patterns that originated from gravity-driven tectonics associated with partial convective overturn of the crust during Paleoarchean [3–7]. On the other hand, tectonic strain in the Neoarchean granite-greenstone terrains is characterized by an anastomosing network of regional transcurrent shear zones indicating heterogeneous strain localization influencing the bulk geometries [8], metamorphism, and exhumation [9–11]. The temporal changes

in heat production and mantle temperatures through the Archean are reflected in a change in the mechanical behavior of the continental lithosphere and its changeover from episodic partial convective overturn in Paleoarchean to horizontal motion of tectonic plates during Neoarchean times [12]. Such transition in the global tectonic scenario by Neoarchean times manifested in a significant increase in recycling of crustal materials into the mantle, emplacement of potassic granitic plutons, and heterogeneous regional strain distribution leading to the development of regional shear zones [13–15]. Also, the Neoarchean record of granite plutonism and the development of heterogeneous strain in shear zones, fluid transfer, and metamorphism are particularly interesting as they are spatially linked to important gold mineralization in many cratons [16, 17]. The Western Dharwar craton (WDC) preserves a unique Paleoarchean dome and keel patterns and Neoarchean regional shear zone network, which offer an excellent opportunity to address, temporal changes in thermo-mechanical processes, and tectonic strain through time [18]. Bouhallier et al. [19] and Chardon et al. [5] described the regional tectonic fabrics and their relationships in the dome and keel patterns from the Western Dharwar craton. Chardon et al. [2], Chadwick et al. [20], and Chardon et al. [18] further studied the sinking basin models and shear zone patterns in the same area. However, in the absence of age-integrated *P-T*-t modelling of Neoarchean-Paleoproterozoic granites, the tectonic significance of crustal-scale shear zones and their spatial relationship to granite plutonism and metamorphism remains poorly constrained. This contribution addresses the spatial and temporal relationships between shear zone development, metamorphic *P-T* paths, and emplacement of Koppa granite within the framework of Neoarchean tectonics of the Western Dharwar craton.

2. Regional Geology

The Dharwar craton preserves a large section of pristine Archaean continental crust, forming a wide time window for early Earth dynamics. Numerous studies by Chadwick et al. [20], Bouhallier et al. [19], Chardon et al. [18, 21], Vijay Rao et al. [22], Jayananda et al. [23], and several other workers have contributed to our understanding of fundamental architecture, accretionary processes, and craton building processes of the Western Dharwar craton. A comprehensive complication of available literature by Jayananda et al. [24, 25], Corfu and Hegde [26], and Ao et al. [27] reveals that this craton is made of three major lithological associations, including vast areas of TTG-type gneisses (Peninsular gneisses), two generations of volcano-sedimentary greenstone sequences (older ca.3400-3200 Ma Sargur group and younger ca.3000-2600 Ma Dharwar supergroup), and three generations of calc-alkaline to potassic granites (ca. 3000 Ma, 2640-2600 Ma, and 2550-2500 Ma).

Ramakrishnan et al. [28] subdivided the Dharwar craton into two blocks based on the abundance of granite-greenstone assemblages and metamorphic grade. However, Peucat et al. [29] and Jayananda et al. [30] work on tectonic fabric analysis and metamorphic record. Nd isotope data reveal three crustal blocks, namely, the Western block, Central block, and Eastern block in the Dharwar craton (Figure 1). The Western block preserves the oldest (3600-3200 Ma) basement, classical dome-keel patterns with two major thermal events coinciding with craton forming episodes [31–33]. The Central block comprises a mix of the minor old basement (ca. 3400-3000 Ma) but dominant young (2600-2530 Ma) juvenile crust and was affected by three thermal events (3150 Ma, 2640 Ma, and 2500 Ma). In contrast, the Eastern block contains 2600-2500 Ma juvenile crust that experienced only a 2500 Ma thermal event [29, 34, 35]. The whole Archean crust is affected by significant shear deformation and regional metamorphism close to 2500 Ma, which was immediately preceded by major juvenile magmatic accretion [21, 34, 36]. Tectonic fabric analysis, geophysical data, accretion history, and metamorphic record suggest that all the crustal blocks assembled into a cratonic framework around 2500 Ma [22, 34, 37].

3. Geology of the Study Area

3.1. Regional Geology of the Western Dharwar Craton. The Western Dharwar craton (WDC) contains a well-preserved TTG basement and two-generation greenstone sequences separated by an angular uniformity (Figure 1) [28]. The older Sargur group greenstone successions are composed of mafic volcanics with komatiite lineage interlayered with shallow water sedimentary sequences (conglomerate-quartzite-pelite-BIFs). The younger Dharwar supergroup deposited unconformably on the basement (granitoids and interlayered Sargur group) and comprised the lower Bababudan group and upper Chitradurga group.

The Bababudan group starts with an oligomictic conglomerate [38], followed by thick basaltic lava flows. The basaltic flows are interlayered with quartzites, showing cross-bedding, followed by phyllite-tuff-BIFs towards the summits [39]. A detailed strain fabrics mapping and kinematic analysis of the Bababudan basin demonstrate a radial centripetal collapse of high-density greenstones into low-density gneiss basement with strain localization confined to the decollement at the contact with basement and greenstone sequence [18]. The younger Dharwar supergroup is represented by the ca. 2700-2650 Ma Chitradurga greenstone belt and ca. 2635-2605 Ma Shimoga-Dharwar basin [40, 41]. These greenstone sequences start with polymict conglomerate followed by basaltic flows, intermediate to felsic volcanic flows, and shallow- to deep-water carbonate-greywacke-argillite-carbonaceous-shale-BIF sequences [20, 30, 34, 42]. These Chitradurga–Shimoga greenstone sequences are intruded by ca. 2620-2600 Ma granite plutons [24, 43].

Earlier studies imply that the WDC was affected by regional shortening associated with strain localized along with major widely spaced north-south trending shear zone networks [18, 44]. These shear zones run from amphibolite-granulite-transition in the south and are traversing the greenschist facies greenstone-granite terrains to the north and finally concealed by the Deccan volcanic province. The major shear zones include the anastomosing shear zone network that traverses the Chitradurga greenstone belt, the shear zone traversing the Holenarsipur and Bababudan greenstone belt's eastern boundary, and the Balehonnur shear zone that traverses

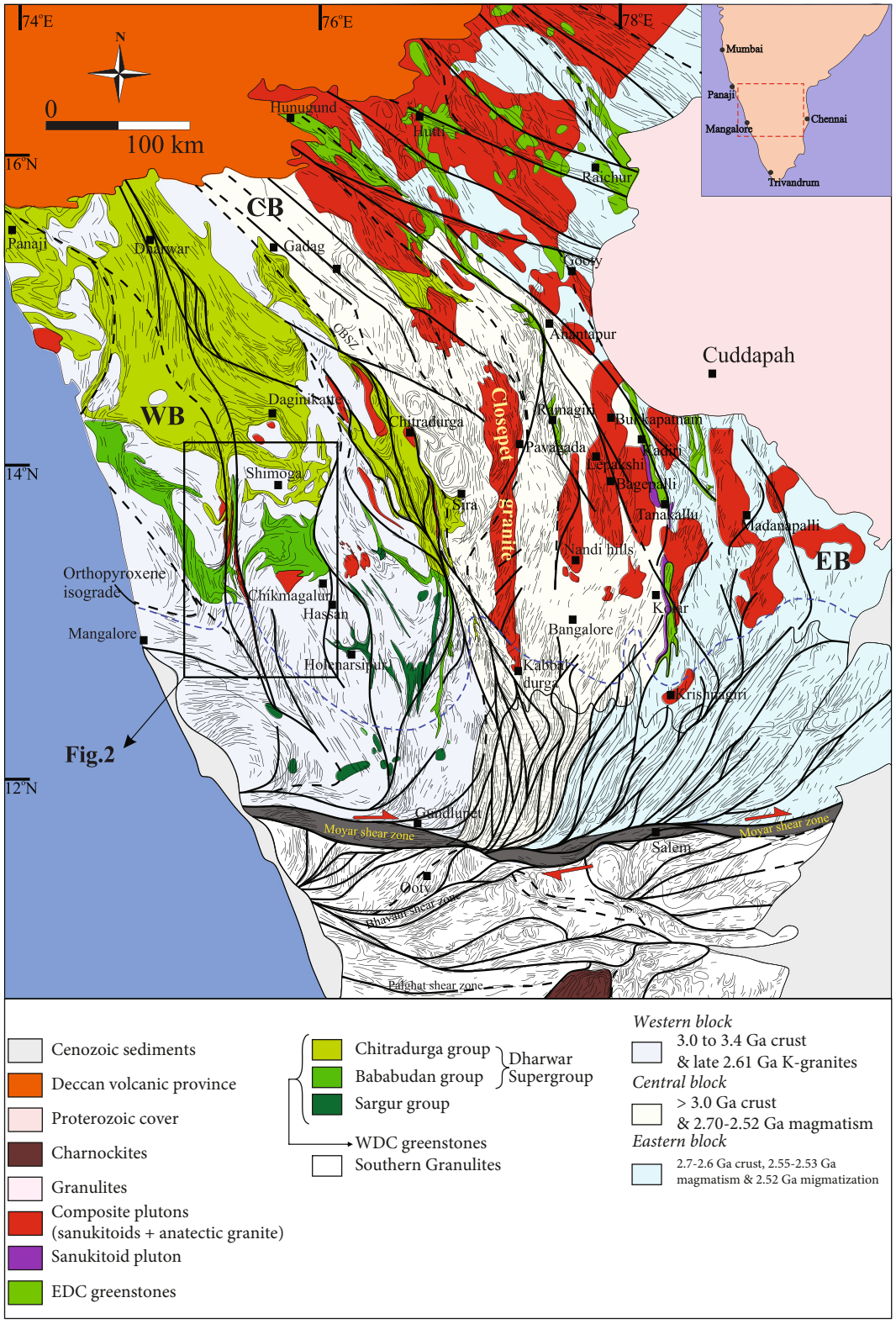

Figure 1: Regional geological map of Dharwar craton [after 18,21,23].

contact zones of the Bababudan, Shimoga, and Kudremukh greenstone belts (Figure 1 [18]). The present study focuses on the Balehonnur shear zone covering a crustal corridor from Koppa in the north to Kottigehara in the south (Figure 2).

3.2. The Balehonnur Shear Zone. The Balehonnur shear zone (Figure 2) is a major north-south trending crustal-scale shear zone network (about 400 km in length and 5-15 km width) with a sinistral sense of displacement that traverses

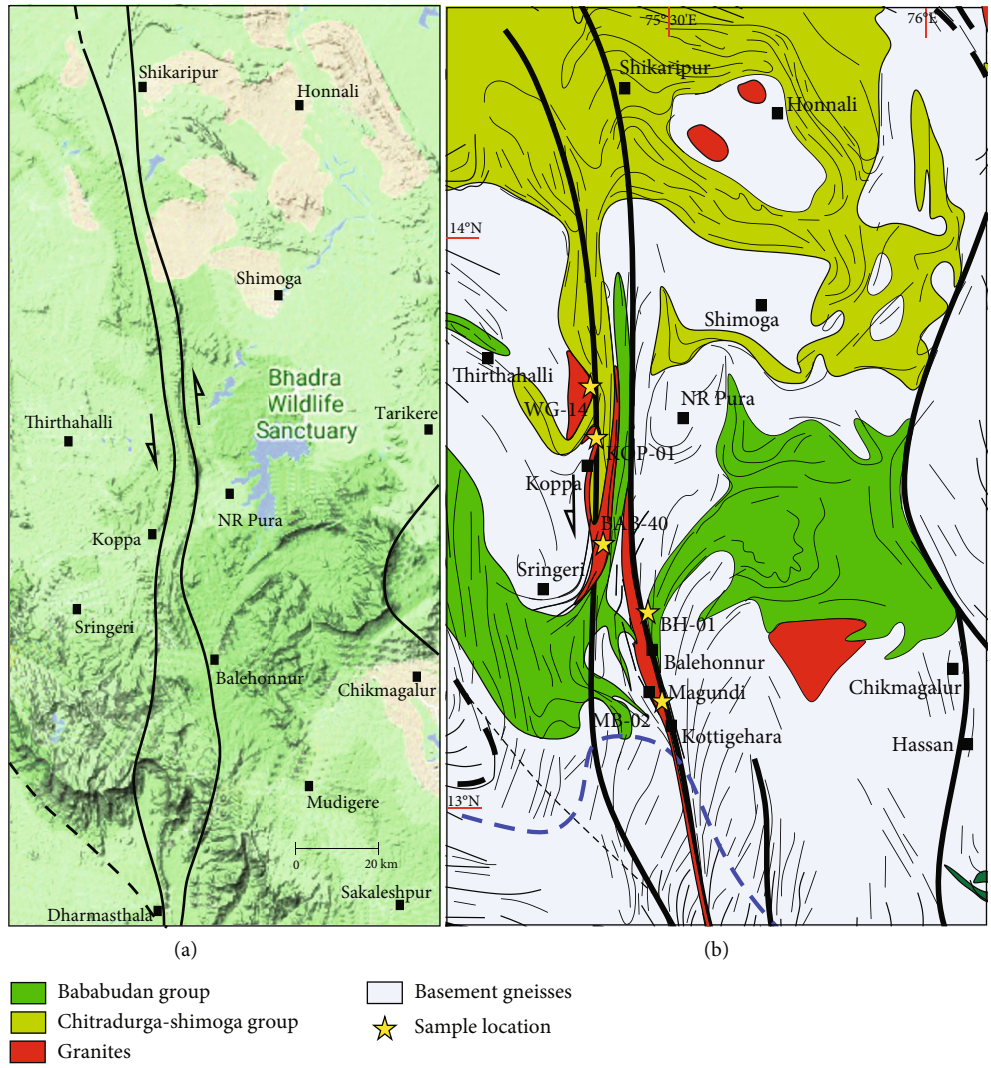

FIGURE 2: (a) Google terrain map of the studied corridor and (b) geological sketch map of the Balehonnur shear zone with fabrics data.

the largest preserved section of Archean crust in the WDC [2, 18]. This shear zone is exposed from the southern margin of the craton and extends to the north up to Goa and is concealed under Deccan lava flows further north [2, 18, 45, 46]. In the southern part of the WDC, the WNW trending Kasaragod-Mercara shear zone is transposed into the Balehonnur shear zone, and the southernmost tip of the latter is deflected into the Moyar shear zone [18]. The Balehonnur shear zone separates Bababudan greenstone in the east, Western Ghats greenstone belt (Kudremukh belt), and Shimoga basin to the west (Figure 2). A significant part of the Shimoga basin is found within the shear zone and affected by high-shearing strains, as revealed by the decrease in the width of the greenstone sequences and intense stretching of the greenstone assemblages (Figure 3(a)). Detailed satellite image analysis, field mapping, and kinematic analysis revealed a sinistral motion in this shear zone [18, 46]. The reduction in thickness of Bababudan, Shimoga, and Kudremukh greenstone sequences, together with TTGs and potassic pluton (Koppa granite), can be observed in the shear zone. The Koppa granite exhibits a vertical to oblique NNW trending foliation with horizontal to shallow-plunging lineation (Figure 3(b)). Based on field observations along the selected corridor, an increase in strain could be inferred by a grain size reduction, intense stretching of constituent minerals, and recrystallization of the greenstone volcanics, TTGs, and granites that ultimately lead to mylonite to ultramylonite formation (Figure 3(c)). Jayananda et al. [34] previously correlated this shear zone's temporal and spatial evolution with regional metamorphism through slow cooling that affected the entire Western Dharwar craton during ca. 2.5-2.40 Ga ([34]). Within the greenstone volcanics, shear deformation is spatially associated with metamorphic recrystallization with upper greenschist–lower amphibolite facies garnet-hornblende–actinolite assemblages (Figure 3(d)). The extensively deformed portion (referred as core) of the shear zone comprises mylonite to ultramylonite (see Figure 3(c)). In the deeper levels of the shear zone (south of Kottigehara in Charmadi Ghat–Shiradi Ghat section), a progressive increase in metamorphic grade from lower amphibolite–upper amphibolite facies garnet-biotite-plagioclase assemblage is developed (Figure 3(e)).

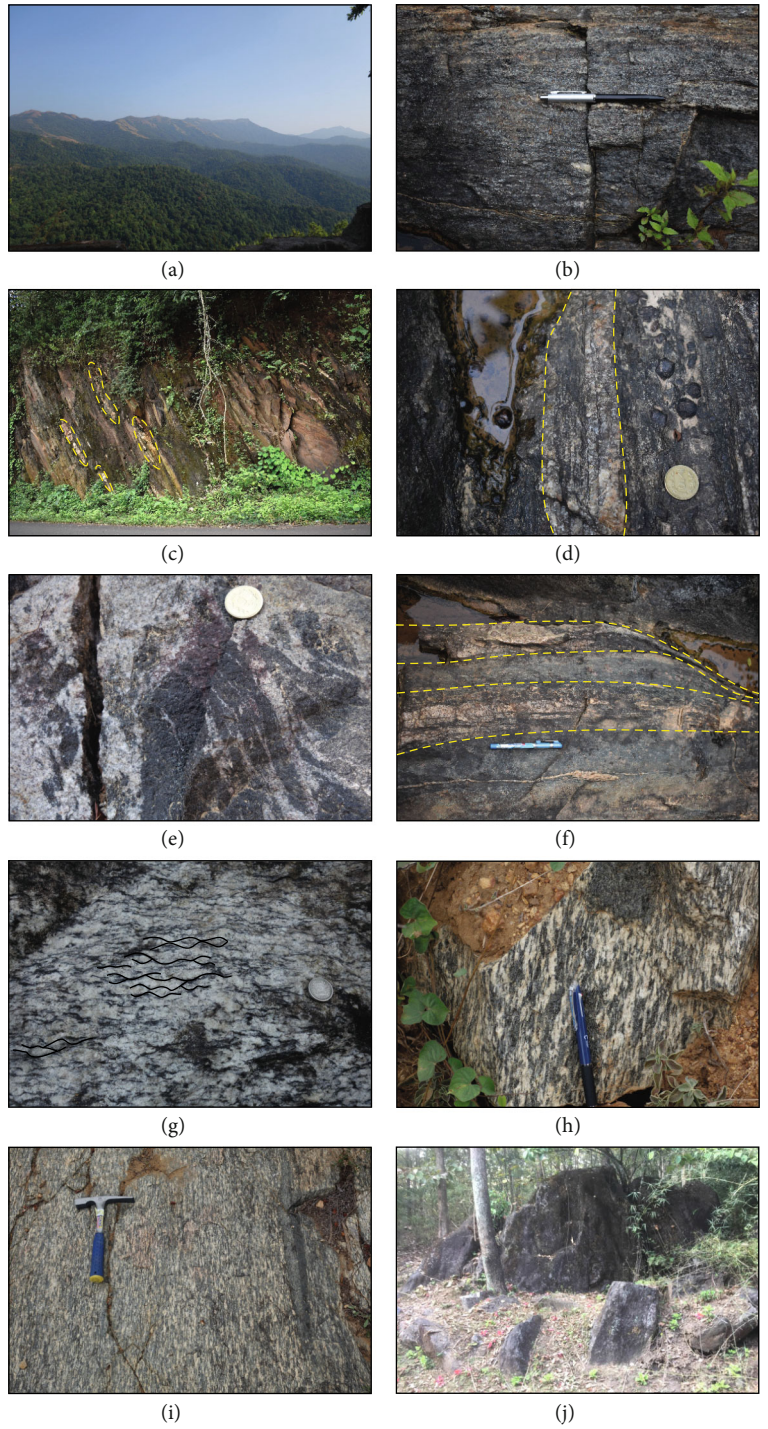

FIGURE 3: Field photographs. (a) Panoramic view of Balehonnur shear zone. (b) Garnet-bearing amphibolite containing small feldspar-quartz. (c) Mylonite in Balehonnur shear. (d) Large garnet crystals close to granite veins in mafic rocks. (e) TTGs with mafic boudins SW Kottegehara. (f) Koppa granite vein boudinaged within mafic volcanics containing garnet. (g) Koppa granite showing C-S fabrics. (h) Koppa granite showing C-prime fabric. (i) Mylonitic Koppa granite. (j) Transformed garnet-biotite rock near Magundi.

3.3. The Koppa Granite. The Koppa granite pluton, including geological and fabric maps, is poorly known due to dense vegetation cover. This study focused on the crustal corridor covering Koppa-NR-Pura in the north and Kottigehara in the south (see Figure 2). We have made several traverses along road sections, particularly on small roads in coffee plantations and forest, to understand the extent of the pluton and fabrics of the constituent mineral phases in the pluton. In the field, Koppa granite is found as an elongated N-S trending pluton along the contact zone with Kudremukh (Western Ghats belt)-Shimoga–Bababudan greenstone belts. Due to dense vegetation, poor outcrops, and intense shear

deformation, the nature of contact between Koppa granite and adjoining greenstone assemblages is not clear. However, intrusive relationships, as marked by granitic veins within the greenstone volcanics, can be observed at the outcrop scale (Figure 3(f)). On the latitude of Koppa, outside the shear zone, the granite is less deformed and shows a weak foliation defined by the alignment of amphibole and biotite. However, granite pluton shows a progressive increase in plastic deformation towards the core of the shear zone and is marked by prominent foliation defined by the alignment of mafic minerals, stretching of feldspars followed by C-S and C-prime structures (Figures 3(g) and 3(h)). With a further increase in strain, the granite transforms into mylonite (Figure 3(i)) and eventually to ultramylonite (see Figure 3(c)). Towards south in the Magundi region within the central part of the shear zone, the Koppa granite was completely recrystallized and transformed into garnet-biotite rock (Figure 3(j)) with rare feldspars, possibly indicating garnet formation by consuming plagioclase and biotite during eclogite-high *P* granulite facies metamorphism [9, 10, 47].

Further south, in the Kottigehara-Charmadi Ghat section, the shear zone displays steep ductile fabrics in migmatitic TTGs containing garnet-clinopyroxene bearing mafic boudins, in turn, traversed by granite veins of possible Koppa granite affinity along foliation (see Figure 3(e)). Further south in the Shiradi Ghat section, typical granulite facies assemblages with orthopyroxene are preserved [48–50], which is beyond the scope of the present study.

4. Analytical Methods

4.1. Electron Probe Microanalysis. Representative back-scattered electron images (BSE) of silicate phases were acquired using a scanning electron microscope (SEM) installed at the Indian Institute of Science Education and Research in Bhopal. The analytical conditions for BSE imaging are as follows: accelerating voltage of 20 kV and filament current: 400 picoamperes (pA). The silicate minerals in studied samples were analyzed using a 5 WDS CAMECA SX-100 electron probe microanalyzer (EPMA) at Central Petrological Laboratory, Geological Survey of India. The accelerating voltage was set to15 kV in a LaB_6 cathode with a beam current of 15 nA and beam diameter between 1 and 5 μm for silicate analysis. The following natural mineral standards are chosen for analysis: MgO for Mg, apatite for Ca, hematite for Fe, rhodonite for Mn, orthoclase for K, rutile for Ti, albite for Na and Si, and almandine for Al. The analytical errors and reproducibility are within the limits mentioned in Camaca Standard Operating Procedure for SX-100.

4.2. Major and Trace Elements. Major and trace element contents of the studied samples were determined by utilizing an X-ray fluorescence spectrometer and a high-resolution inductively coupled plasma mass spectrometer installed at CSIR-National Geophysical Research Institute Hyderabad. The analytical protocols, including reference material and associated errors, are after Krishna et al. [51] and Satyanarayanan et al. [52], respectively.

4.3. U-Pb Zircon Geochronology. Zircon crystals were imaged by cathodoluminescence or back-scattered electrons using SEM and dated by U-Th-Pb isotope measurements done by LA-ICP-MS at Laboratoire Magmas et Volcans (Université Clermont Auvergne, France), using the same analytical facility and conditions as described in Jayananda et al. [25] and Guitreau et al. [53]). The reference material 91500 was used as an external standard for instrumental fractionation correction, and AS3 and Plešovice zircons were used as secondary standards for data quality check. The laser frequency was set to 4 Hz for the analytical session, laser fluency to 2.5 $J.cm^{-2}$,' and spot size to 33 μm. Zircon crystals were analyzed from two samples, WG-14 and 18 MB-02, the latter of which only yielded one pristine crystal. The Zircon reference material 91500 gave a Concordia age of 1066.5 ± 3.1 Ma (2σ), consistent with the reference 1065 Ma [54]. Similarly, AS3 and Plešovice reference material gave Concordia ages of, respectively, 1093.8 ± 4.2 Ma (2SE) and 334.3 ± 3.9 Ma (2SE), consistent with the ages of 1099 and 337 Ma, as reported in Paces and Miller [55] and Sláma et al. [56], respectively.

5. Data Reduction

5.1. Electron Probe Microanalysis. The structural formula and representative chemical analysis of the current set of samples were calculated using A-X software (http://ccp14.cryst.bbk.ac.uk/ccp/web-mirrors/crush/astaff/holland/ax.html).

The mineral chemical data and its representative chemical formulae are given in Appendix 1. Mineral abbreviations are after Whitney and Evans [57].

5.2. Classical Thermobarometry. Empirical formations involving Fe-Mg exchange between garnet and biotite were used to constrain the peak temperature of the studied samples experienced during metamorphism. As plagioclase grains are rare in the studied sample, the equilibrium pressure estimation using the chemical composition of coexisting garnet, biotite, plagioclase, and quartz is uncertain. Still, the garnet-biotite-plagioclase-quartz barometer [58] is utilized to calculate the equilibrium pressure for reference,

In contrast to the garnet-biotite schist (sample 18 MB-02), empirical formulations involving garnet and calcic-amphibole could not be utilized as the measured compositions of amphiboles were mostly grunerite—cummingtonite and plotted outside the calibrated amphibole composition. Thus, phase equilibria diagrams using appropriate bulk composition are constructed to constrain the studied samples' prograde, peak, and *retrograde P-T* conditions.

Also, the temperature (T_{Zr}) of granitic magma emplacement can be estimated using an empirical formulation of Watson and Harrison [59] and Boehnke et al. [60], respectively.

5.3. P-T Pseudosection Analysis. The FORTRAN program package, PERPLE_X (version 6.9.1, compiled on 20-4-222), was utilized for the phase topology modelling in the NCKFMASH system [61]. The thermodynamic properties of mineral phases are taken from hp633ver.dat and its

subsequent modifications after Holland and Powell [62]. Quartz is set to present as excess. As the Fe^{3+}/Fe^{total} ratio is uncertain from-XRF analysis, all Fe is assumed to be in Fe^{2+} in calculations.

For the garnet-biotite gneiss sample, the following activity-composition solution models were used in the phase-topology modelling: garnet [63], biotite [64], plagioclase [65], orthopyroxene [66], and granitic melt [67]. Since the studied sample contains alkali feldspar and biotite, the amount of H_2O is fixed from the relative modal proportions of these minerals. Accordingly, fifteen thin sections chosen randomly from the same sample were examined in a scanning electron microscope to get the relative proportions of biotite and alkali feldspar. In the next step, the studied sample's total K_2O (mol.) content is adjusted between K-feldspar and biotite as per their relative abundances. As biotite stoichiometry contains water twice the cations in the A-site [68], H_2O is fixed as twice K_2O content estimated from volume portions of biotite to make the system just water saturated for biotite stabilization.

For the garnet-amphibolite bearing enclave solution, models consistent with the melting of mafic rocks are chosen for equilibrium phase diagram modelling. The activity composition models for monoclinic amphibole were taken from Green et al. [69]. Accordingly, the garnet and silicate melt models are taken from Holland et al. [70].

Initially, the whole-rock bulk composition is used to construct *P-T* conditions. We correlate the predicted and observed mineral assemblages in the whole-rock phase diagram. In case of a discrepancy, the *P-T* pseudosection is again constructed using microdomain bulk rock composition, as local reaction equilibrium seems to be more practical and realistic for rocks with relatively fewer H_2O-rich minerals [71].

The following compositional parameters are modelled to constrain the *P-T* conditions: anorthite mol. % [Ca/Ca + Na) × 100] for plagioclase, Mg mol.% [Mg/(Mg + Fe) × 100] for biotite, pyrope mol.% [Mg/Ca + Mg + Fe) × 100], grossular mol.% [Ca/Ca + Mg + Fe) × 100], and almandine mol.% [Fe/Ca + Mg + Fe) × 100] for garnet.

5.4. Geochemical Analysis. GCDKIT [10] is used to plot geochemical data. The major trace and rare-earth-element data is given in Appendix 2. The individual temperature and pressure estimates calculated from zircon solubility in are silicate melt [59, 60], and normative silica-albite orthoclase content [72] is shown in Appendix 2.

5.5. U-Pb Zircon Ages. Data reduction was made using Glitter software [73]. The U-Pb Concordia plots and age calculations were done using Isoplot [74]. The geochemical data are shown in Appendix 3.

6. Results

6.1. Petrology. Details of studied samples from Balehonnur shear zone including GPS location, rock types, and mineral assemblages and ages are presented in Appendix 4. Similar to the undeformed Koppa granite mineralogy, quartz > K-feldspar > > plagioclase, in order of decreasing abundances, constitutes the primary magmatic minerals in the garnet-biotite schist (Figures 4(a) and 4(b)). Blastoporphyric garnet and biotite are metamorphic minerals in the studied samples (Figure 4(c)). Zircon and titanite are the accessory minerals. Quartz grains exhibit undoes extinction (Figure 4(a)) and wavy grain boundaries (Figure 4(b)). The blastoporphyric garnets are mostly subhedral–euhedral and contain rounded inclusions of biotite and quartz (Figure 4(c)). Inclusions of plagioclase feldspar are rare within blastoporphyric garnet. Quartz along the garnet boundary is cuspate-shaped, implying their crystallization from melts (marked as while a box in Figure 4(c)) [75–78]. Most of the garnet grains are homogeneous in composition, with the composition tightly constrained between Alm ($_{core\text{-}rim}$) mol. %: 66–68, Pyp ($_{core\text{-}rim}$) mol. %: 12-14, and Grs ($_{core\text{-}rim}$) mol. %: 16-18 with Sps content <2 mol. %. Locally biotite grains overgrow the garnet grains along cracks.

The biotite Mg mol. % and TiO_2 content are tightly constrained between 44–46 and 2.45–2.85 wt.% (11 O p.f.u), respectively. Plagioclase grains are rare in the studied samples. Only a single grain with plagioclase composition, a mol. % =36, is observed during the present study; the paucity of the plagioclase grains implies that most of the grains are consumed during garnet stabilization (discussed later in the *P-T* pseudosection chapter).

Deformed plagioclase, garnet, and fibrous amphiboles are major constituent phases in mafic enclaves (21BH-01) within the granite. In the less retrogressed variety, garnet-clinopyroxene–amphibole assemblage is preserved (Figure 4(c)). Large blastoporphyric garnets (average diameter 250–300 μm) are the only metamorphic mineral present in the samples (Figures 4(d)–4(f)). Amphibole, quartz, and occasionally feldspar are present as inclusion phases within the garnet.

The amphiboles belong to the grunerite–cummingtonite series with Si (23 O a.p.f.u) and Mg mol.% of the analyzed grains vary between 6.52 to 6.90 and 58 to 59, respectively. The plagioclase from the present study mostly andesine-oligoclase in composition (An mol.% =32-34). The blastoporphyric garnets are mostly homogeneous (Alm: 71-73, Pyp 16-19, and Grs 9-11), with end member chemical compositions varying between 2 mol.% within an individual grain. The retrograde textures, i.e., the formation of hydrous minerals over granites, are not developed in the rocks, implying the lack of water during cooling.

6.2. P-T Estimation

6.2.1. Magmatic Temperature. The T°C (T_{Zr}) estimation for the undeformed granite samples is constrained between 821°C–1022°C and 827°C–1027°C if the formulation after Watson and Harrison [59] and Boehnke et al. [60] is utilized, respectively. The temperature estimations are higher than general cut-off temperature, i.e., 830°C, for A-type granites [79, 80]. For the undeformed granites and garnet-biotite gneisses, the T_{zr} is a first-hand information about the magmatic crystallization temperature of

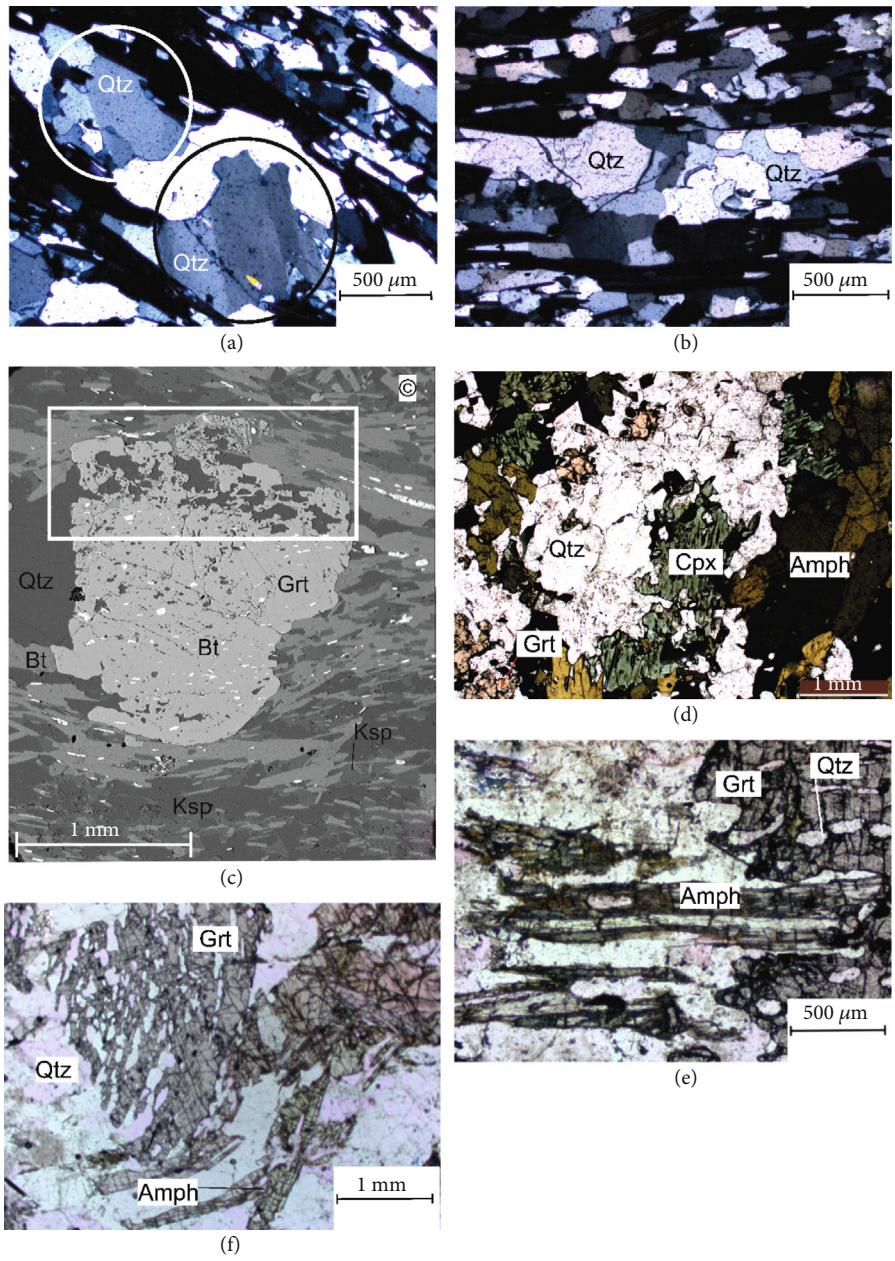

FIGURE 4: Photomicrographs of reaction microstructure. (a) Crossed polar photo micrograph showing chess-board (undulose) extinction in quartz (marled by unfilled white circle). (b) Quartz-biotite defined fabric in the deformed Koppa granite. The quartz-ribbons show wavy grain boundary, implying grain boundary migration accommodated recrystallization. (c) Back-scattered electron image showing garnet growth over biotite defined fabric. Quartz microstructures resembling recrystallization from incipient melt is marked by a white box. (d) Crossed polar photomicrograph of plagioclase- clinopyroxene – amphibole bearing mafic enclave. (e–f) Plane polar photomicrograph showing blastoporphyric garnet growth over amphibole-quartz defined fabric. Amphibole, quartz, and occasionally feldspar are present as inclusion.

undeformed Koppa granite. Without a suitable magmatic geobarometer, the depth for magma emplacement could not be determined.

6.2.2. Metamorphic Pressure–Temperature Conditions. As the blastoporphyric garnets are primarily homogeneous, chemical composition from garnet–biotite pair which is not in contact yield 700-725°C, between 0.4 and 1.4 GPa, if formulations after Holdaway et al. [81] are used. However, a modified formulation by Holdaway [82] yielded a relatively higher peak temperature of 750–775°C, between 0.4 and 1.4 GPa. As the temperature differences (50°C-70°C) are very close to the general analytical uncertainties, ±50°C [83, 84], we suggest the peak metamorphic temperature estimates involving garnet-biotite pairs are consistent when two different formulations are involved. The chemical formulations of coexisting garnet–biotite–plagioclase–quartz barometer yield pressure 0.9–1.0 GPa [58].

The chemical composition of amphiboles in the studied mafic rock sample does not correspond to the calibrated composition of amphiboles in the amphibole–plagioclase thermometer [85] and amphibole-plagioclase barometer [86]. Accordingly, *P-T* conditions are determined by using the stability of phases in *P-T* pseudosection and the intersection of composition isopleths.

6.3. P-T Pseudosection

6.3.1. Sample 18 MB-02. The phase relations using whole-rock bulk composition in the NCKFMASH system for 600˚C to 950˚C and 0.4 to 1.4 GPa for garnet-biotite schist do not predict the stable mineral assemblages similar to those observed in the studied samples (Appendix 1a). The absence of observed mineral phases in the modelled phase diagram implies a different and smaller reaction volume compared to whole-rock reaction volume [71, 87]. Accordingly, reaction volumes are determined by constructing P-X (composition) diagrams at temperatures obtained from garnet-biotite thermometers.

Experimental data by Gardien et al. [88] imply incongruent melting of plagioclase and biotite to stabilize garnet and melt (alkali feldspar–quartz). Accordingly, the two end members (C_o, C_1) are fixed as plagioclase-feldspar and biotite, respectively. The temperature and pressure are fixed at 730˚C (obtained from garnet-biotite thermos-barometry) and 0.4 to 1.4 GPa, respectively. In the P-X (composition) diagram (Appendix 1b), the modelled mineral assemblage, i.e., plagioclase-alkali feldspar–biotite–garnet–melt, similar to the assemblage observed in the present sample is stable towards plagioclase composition end member between 1.0 – 1.2 GPa, implying plagioclase destabilization at higher proportion compared to biotite destabilization during blastoporphyric garnet formation. The higher rate of plagioclase consumption is also reflected by the general paucity of plagioclase grains in the studied sample. In the plagioclase-alkali feldspar–biotite–garnet–melt field, the plagioclase: biotite ratio varies between 0.95: 0.05 and 0.84: 0.16. Thus, to constrain the bulk involving minimum plagioclase and maximum biotite, the effective chemical composition is determined by mixing 0.84 plagioclase and 0.16 biotite (option 1 in the Werami program of Perplex).

In the next step, phase relations using microdomain-bulk composition for 600˚C to 950˚C and 0.4 to 1.4 GPa for garnet-biotite schist are shown in Figure 5. The phase diagram could be divided into three distinct fields based on the mineral assemblages. The mica-bearing assemblage is present in the low *T*–high *P* field. In contrast, orthopyroxene-bearing assemblages are stable in the relatively low *P*–high *T* field.

The magmatic assemblage biotite-plagioclase–quartz is stable between 600 and 700˚C and between 0.4 and 1.6 GPa (Figure 5(a)). Muscovite-bearing assemblages are stable between temperatures 600-700˚C, at pressure >0.6 GPa. As the studied sample does not contain muscovite, the muscovite-in invariant line limits the maximum pressure the rock experienced.

With an increase in temperature >700˚C, biotite destabilizes with silicate melt formation. At temperature ~775˚C, orthopyroxene appears as a stable mineral with plagioclase, biotite, sanidine, and melt. As the rock does not contain orthopyroxene, the *orthopyroxene-in invariant line* marks the maximum temperature the rock has experienced. At pressure ranges >1.0 GPa and 0.8 GPa, between temperatures 700 and 775˚C, garnet becomes stable with plagioclase–biotite–melt and sanidine. As the modelled assemblage, plagioclase–biotite–garnet–sanidine ± melt are similar to those observed in the studied sample, the following conditions, i.e., 700˚C at pressure >1.0 GPa to 775˚C at pressure>0.8 GPa, provide first-hand information about the stability of minerals in the current sample.

The change in the modal abundances of minerals provides vital insight to constrain the progress of metamorphic reactions. The modal abundances of constituent mineral phases are shown in Figures 5(b) and 5(c). The biotite abundance decreases with temperature. Like the biotite modal abundance, plagioclase abundances also decrease with increased temperature. In contrast, garnet, melt, and sanidine modal abundances increase with increased temperature.

The chemical compositions of biotite, feldspar, and garnet are also modelled to constrain the *P-T* condition. The modelled Mg mol.% of biotite and An mol.% of plagioclase, i.e., Mg mol.% =46 and An mol.% =32, intersects at 650˚C, 0.8 GPa (Figure 5(d)). As plagioclase and biotite are the primary minerals for the studied sample, we constrain 650˚C and 1.0 GPa as the equilibrium *P-T* condition. Similarly, the modelled Pyp mol.% and Grs mol.%, similar to those of measured composition, i.e., Pyp mol.% =14 and Grs mol.% =16-18, intersect at 775˚C-800˚C and pressure 1.1-1.2 GPa (Figures 5(e) and 5(f)). The modelled almandine composition of garnet, i.e., 65-66 within the *P-T* window, is similar to the values obtained from electron probe micro-analysis of the representative sample.

The phase diagram predicts ~5 vol% of silicate melt in the *P-T* window defined by the garnet composition. The relatively small melt volume is below the melt percolation threshold [89] and will not be able to form an interconnected melt network to escape from the rock.

6.3.2. Sample 21-BH01. Figure 6 shows the phase relations for garnet-amphibolite schist (21-BH01) in the NCFMASH system. The prograde mineral assemblages similar to commonly observed minerals in mafic rocks, i.e., plagioclase–amphibole, are stable between temperature 650 and 750˚C at pressure 0.8-1.0 GPa. With an increase in temperature >750˚C, silicate melt and garnet appear as a stable phase with amphibole. The mineral plagioclase is stable with garnet–silicate melt–amphibole at pressure<0.8 GPa, and plagioclase destabilizes at pressure >0.8 GPa, at temperature >750˚C. Still, an increase in temperature leads to free quartz dissolution in the silicate melt. Since plagioclase and quartz are present as a stable assemblage in the studied sample, the quartz-out and plagioclase-out univariant reaction lines define the upper limit of the temperature and pressure the rocks have experienced.

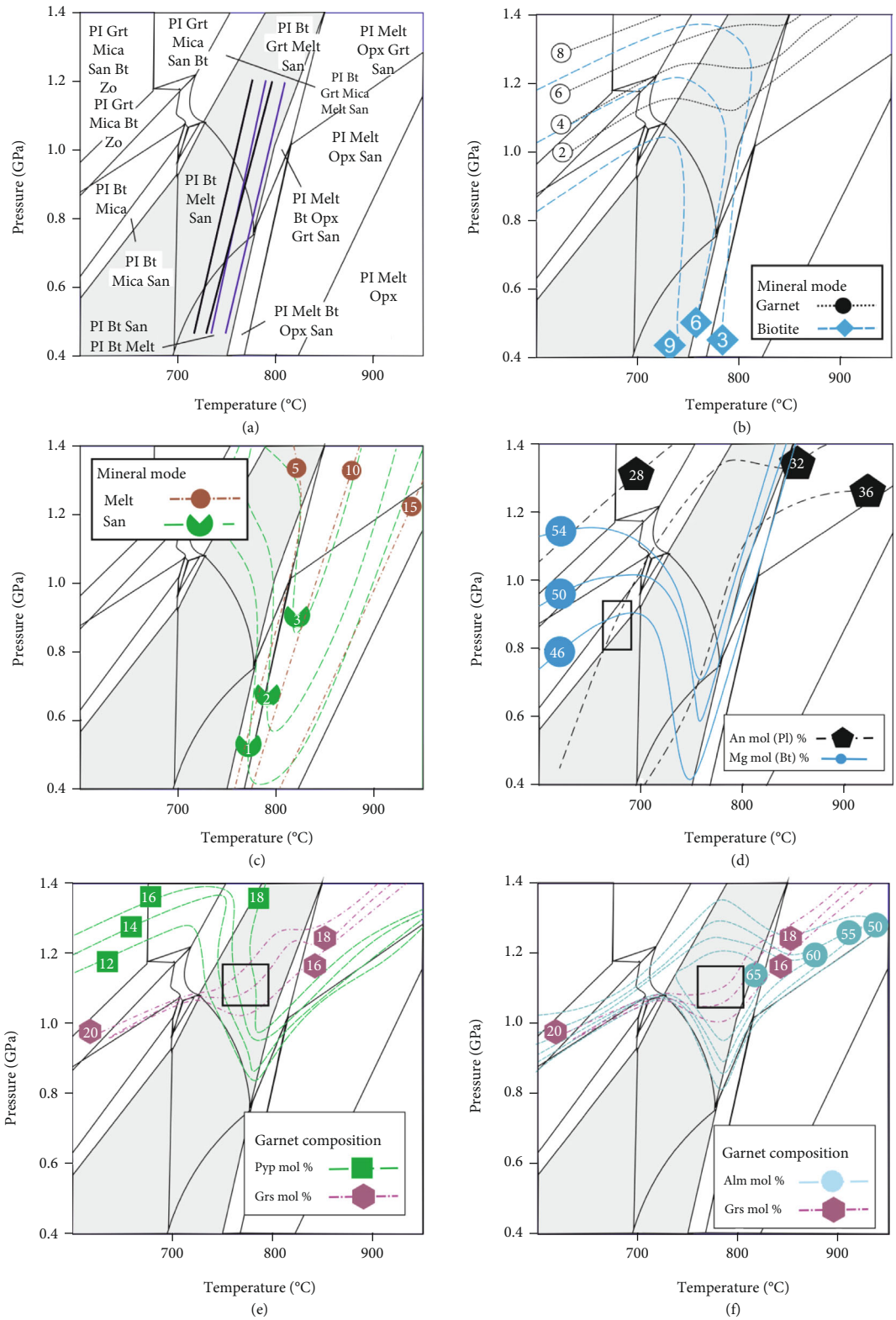

FIGURE 5: Results of *P-T* pseudosection analysis for garnet–biotite bearing granite. (a) NCKFMASH phase topology for 600°C shown to 950°C and 0.4 to 1.4 GPa is shown. (b–c) The modal abundances of garnet-biotite. Melt-sanidine is shown. Intersection of modelled chemical composition of plagioclase, biotite, and garnet is shown in (d) and (e–f), respectively.

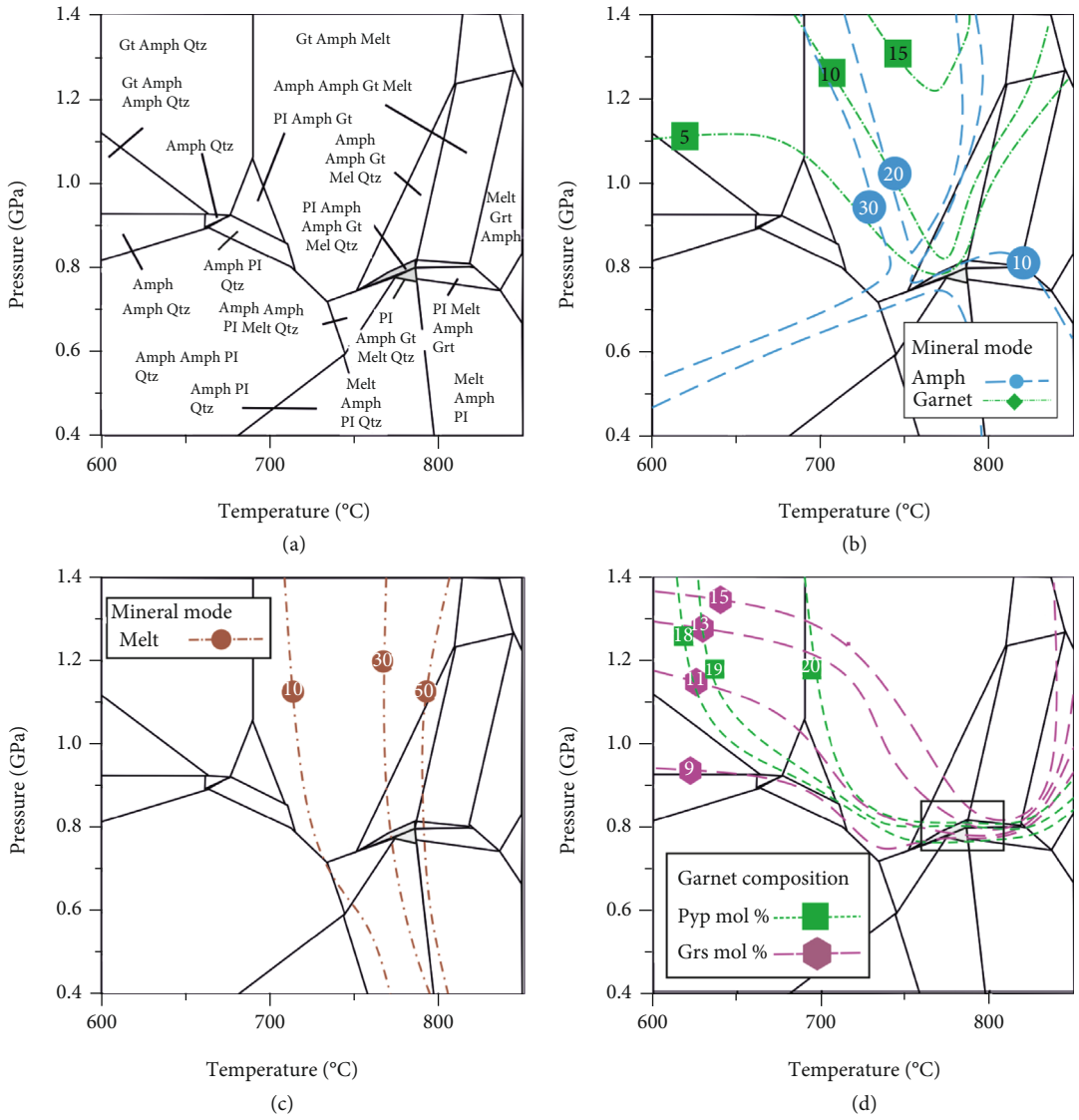

FIGURE 6: Results of *P-T* pseudosection analysis for garnet–amphibole gneiss. (a) NCFMASH phase topology for 600°C to 850°C and 0.2 to 1.6 GPa is shown. (b and c) The modal abundances of garnet, amphibole, and melt are shown. Intersection of chemical parameter of garnet is shown in (d).

The modal abundances for minerals are shown in Figures 6(b) and 6(c). The isopleths showing amphibole modal abundances exhibit a flat slope between 550 and 750°C and a steep slope at temperatures >750°C. The garnet and melt modal abundances increase with an increase in pressure and temperature. In contrast, the amphibole modal abundances decrease with an increase in temperature. The opposite abundances of garnet, melt, and amphibole within 550-750°C imply the formation of garnet via melting of amphibole (discussed later).

The chemical composition of garnet is also modelled to constrain the peak *P-T*. The Pyp content of garnet increases with an increase in temperature. In contrast, the modelled Grs content increase with an increase in pressure. The Pyp and Grs isopleths, similar to those values obtained from the electron probe microanalyzer, intersect at 0.8–1.0 GPa and 750-775°C (Figure 6(c)). In this *P-T* window, the modelled Alm component also matches with the measured chemical composition of garnet (Figure 6(d)).

6.4. Geochemical Data: Major and Trace Elements. Five samples from the shear zone were analyzed for major and trace element contents, and data is presented in Appendix 2. Among the five samples analyzed, four samples are Koppa granites affected by variable shear strain and one sample of garnet-bearing mafic rock involved in shear deformation.

The analyzed Koppa granite samples show significant variation in SiO_2 (69.62-55.53 wt.%), Al_2O_3 (13.34-16.64 wt.%), MgO (1.19-5.82 wt.%), and K_2O (3.92-1.12 wt.%) while garnet-bearing mafic rock displays low SiO_2 (49.74 wt.%), high Al_2O_3 (15.23 wt.%), Fe_2O_3 (12.15 wt.%), and MgO (8.39 wt.%). The Koppa granite contains variable normative quartz (31.03-18.15 mol.%). Mafic rock is also quartz-normative (9.66 mol.%). Three of four analyzed granite samples are peraluminous, and one shows

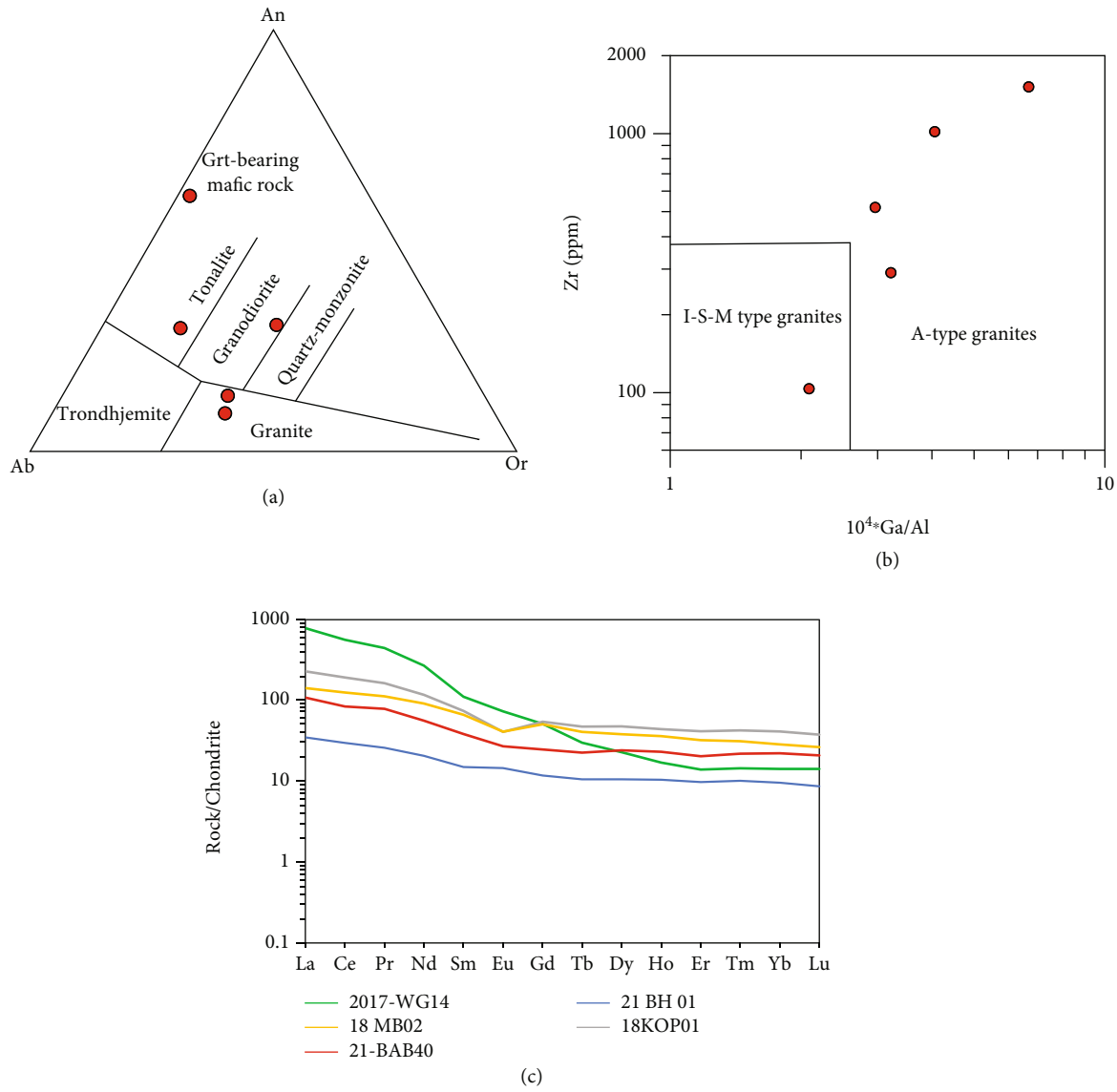

FIGURE 7: Geochemical diagrams. (a) Normative Ab-An-Or triangular diagram (after O'Connors, [111]) with fields from Barker [112]. (b) Zr (ppm) versus Ga/Al discrimination plot of Whalen et al. [91]. (c) Chondrite normalized REE patterns of the studied samples.

a metaluminous character (figure not given). On the Ab-An-Or plot (O'Connor, 1965), the Koppa granite shows tonalite, granodiorite, and granite composition, while the mafic rock plot outside the field (Figure 7(a)).

Among the analyzed Koppa granite, a decrease of LIL elements (K, Rb, Ba, and Sr) content with the increase of shear deformation wherein mylonitic sample (21-BAB 40) show very low-K_2O (1.12 wt%), Rb (9.92 ppm), Ba (48.59 ppm) and Sr (88.39 ppm) is observed. Other less deformed samples show higher LIL element contents (K_2O = 2.90-3.92 wt%; Rb = 72.52-219-91 ppm; Ba = 412-1179 ppm; and Sr = 132-715 ppm). This observation suggests that LIL element's content is affected by strong shear deformation, metamorphism, and associated fluid flow. The high fluid pressure associated with metamorphism and deformation in the core of the shear zone probably flushed the LIL elements and shifted to higher structural levels in the crust. Earlier, Newton [90] documented that higher content of LIL elements in shear zones rocks is linked to fluid flow.

On the other hand, all the analyzed Koppa granite samples exhibit high HFS elements (Zr = 290.5-1515.0 ppm; Hf = 7.08-37.60 ppm; Nb = 16.87-23.50 ppm; Ta = 1.50-8.07 ppm; Y = 35.57-88.62 ppm; Th = 7.19-40.08 ppm; and U = 0.91-3.04 ppm), and it appears that HFS elements were not affected by shear deformation, metamorphism, and fluid flow. The high HFS element contents together with high Y/Nb (>2.1; c.f Nelson Eby, 1990) and Zr versus 10^4*Ga/Al plot (Whalen et al., [91]) indicate A-type granite (Figure 7(b)). The analyzed garnet-bearing mafic rock is characterized by low contents of LIL elements (Rb = 7.74 ppm; Ba = 44.01 ppm; and Sr = 144.93 ppm) and moderate HFS elements (Zr = 103 ppm; Hf = 2.69 ppm; Nb = 4.49 ppm; Ta = 0.47 ppm; Y = 20.17 ppm; Th = 2.13 ppm; and U = 0.53 ppm).

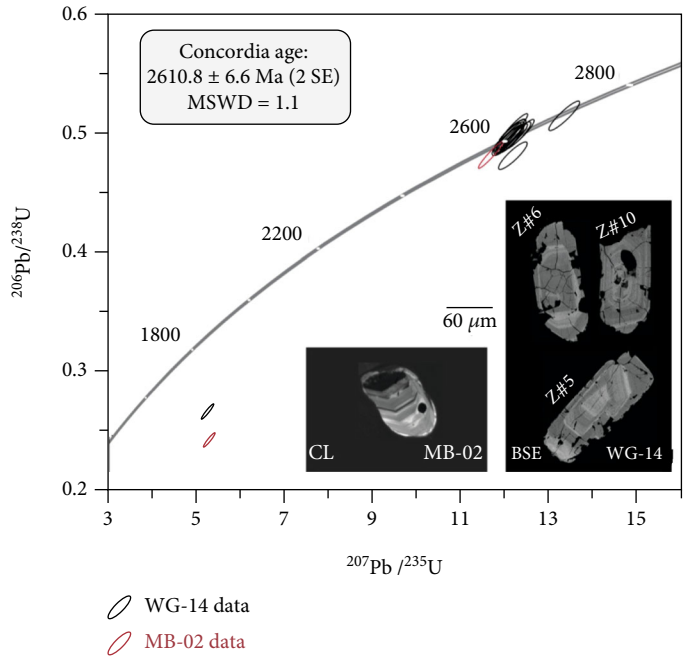

Figure 8: Zircon U-Pb Concordia plot of 18 MB-02 and 17WG14.

The Koppa granite samples contain high to very high total REE (391-975 ppm). In contrast, the mafic rock contains low total REE (67.0 ppm). The granite samples show poorly to highly fractionated REE patterns $[(La/Yb)_N = 5.55 - 55.40]$, with two samples showing minor negative Eu anomalies (Figure 7(c)). The garnet-bearing mafic rock displays moderately fractionated REE patterns $[(La/Yb)_N = 3.63$ and $(Gd/Yb)_N = 1.23]$ with slight positive Eu $(Eu/Eu^*) = 1.10$.

6.5. U-Pb Zircon Ages. Zircon crystals from WG-14 exhibit fine broad faint oscillatory zoning from core to rim. In some grains, a metasomatic alteration can be seen. Some crystals contained inclusions that were avoided during analysis. The only pristine crystal recovered from MB-02 shows fine oscillatory zoning from core to rim. As visible in Figure 8, most U-Pb data obtained on WG-14 zircons are concordant and cluster at a Concordia age of 2610.8 ± 6.6 Ma (2σ).

Two data points indicate slightly older ages of ~2700 Ma and plot to the right of the main cluster. Only one analysis of WG-14 returned very discordant data that was not considered for age calculation. The zircon recovered from 18 MB-02 was analyzed twice and gave a very discordant analysis and near concordant one corresponding to an age of 2594 ± 17 Ma (2σ), which is consistent with that of the WG-14 main cluster within analytical uncertainty. Discordant zircons were also those with the highest U and Th contents, but they did not show a different Th/U compared to other zircons. It should be noted that zircon crystals consistently exhibit Th/U values, i.e., 0.7 to 2.0, which is mostly higher than typical magmatic zircons (~0.2-1.0) [92, 93].

We interpret the age of 2610.8 ± 6.6 Ma (2σ) as the best estimate for the timing of crystallization of WG-14 and 18 MB-02, and the slightly older ages may represent crystals inherited from a slightly earlier event.

7. Discussion

7.1. Metamorphic P-T Evolution of Balehonnur Shear Zone

7.1.1. Sample 18 MB-02. The opposite trend of garnet–melt–sanidine and biotite implies that garnet formed via consuming biotite ± plagioclase ± quartz in water undersaturated/just saturated conditions following reactions [88, 94]

$$\begin{aligned}&\text{Biotite} \pm \text{Quartz} \pm \text{Plagioclase} \rightarrow \text{Garnet} + \text{Sanidine} + \text{Liquid},\\&\text{Biotite} \pm \text{Quartz} \pm \text{Plagioclase} \pm \text{Sanidine} \rightarrow \text{Garnet} + \text{Liquid}.\end{aligned} \quad (1)$$

7.1.2. Sample 21BH-01. Patino Douce and Beard [95] suggest that the amphibole dehydration reaction occurs over a wide range of temperatures, depending on the amphibole (protolith) composition. Different anhydrous phases may accompany the reaction. The complete absence of calcic amphibole in the present sample implies a complete destabilization of hornblende during prograde metamorphism, leaving blastoporphyric garnet and monoclinic amphibole (grunerite–cummingtonite) as a restite [96]. Accordingly, the following reaction is suggested for the formation of garnet-amphibolite [95].

$$\begin{aligned}\text{Calcic Amph}_{\text{I}} + \text{Pl} - > \text{Silicate Melt} \pm (\text{Cpx} - \text{Opx})\\ + \text{Moniclinic Amh} + \text{Garnet} (\text{at } P > 0.8\,\text{GPa}).\end{aligned} \quad (2)$$

7.2. P-T Path Reconstructions. The temperature estimates from zircon solubility, reaction microstructure, and *P-T* conditions estimated from phase equilibria modelling enable us to derive the *P-T* path of the present sample.

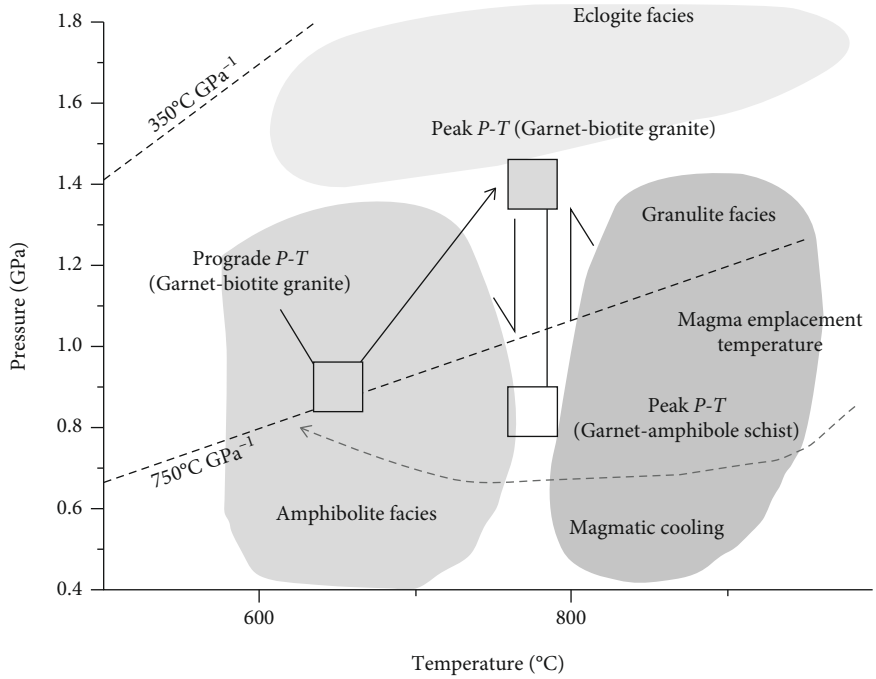

FIGURE 9: Reconstructed *P-T* path for the studied samples. Cooling from the igneous emplacement condition is shown by a broken arrow. The *P-T* conditions for the studied samples are shown by unfilled box, which is exaggerated slightly for a better clarity.

The magmatic temperature (Tz_r) is estimated to be >1,000°C for the undeformed granites. When plotted in a *P-T* path, the peak magmatic temperature (T_{zr}) and prograde path define a phase of initial cooling and hydration leading to the stabilization of biotite (Figure 9).

The prograde *P-T* and peak *P-T* conditions, i.e., 650°C, 0.8 GPa, and 775°C-800°C, and 1.0–1.2 GPa, define a clockwise *P-T* path for garnet–biotite bearing samples (18 MB-02) from the Balehonnur shear zone. However, the samples of the present study do not exhibit the retrograde reaction texture, which implies a lack of water during retrogression. Conversely, the garnet-amphibolite bearing sample (21BH-01) from the same shear zone yielded garnet crystallization *P-T* conditions as 750°C and 0.8 GPa.

Compared with the modelled geothermal gradients of Brown [10], the peak conditions from garnet-biotite schist imply garnet stabilization by consuming biotite and plagioclase occurred in the eclogite-high P granulite facies *P-T* condition (Figure 9). In contrast, the garnets from garnet-amphibolite schist are formed in a shallow depth and at a nearly similar temperature. The estimated *P-T* conditions from garnet-biotite schist and garnet-amphibole schist imply an increase in the pressure gradient from garnet-amphibole mafic rock to the garnet-biotite rock towards the southern part of the shear zone in the studied corridor.

7.3. Relationship between Pluton Emplacement and Shear Zone Development. Calc-alkaline to potassic plutons are spatially associated with crustal-scale transcurrent shear zones documented worldwide [44, 97]. In the northern part of the studied corridor (Koppa-N.R. Pura section), outside the shear zone, the Koppa granite displays poorly developed foliation with coarse-grained equigranular to porphyritic textures, which show a progressive increase in deformation towards the shear zone as reflected in plastic strain characterized by the reduction in grain size and strong preferred orientation of constituent minerals (see Figure 3(h)) followed by C-S/C-prime fabrics and eventually mylonite to ultramylonite. These plastic fabrics argue that granite was already crystallized at the time of initiation of regional shear zone development ca. 2547 Ma, as revealed by U-b monazite ages in the adjacent regions of the WDC (Rekha et al., [98]). As chess-board twinning in quartz is considered a characteristic high-temperature deformation feature (>650°C, [99]), the presence of the same in the studied sample also implies shearing initiation at temperature ~650°C. The estimation of prograde *P-T* condition for the plagioclase-biotite assemblage at 650°C and 0.9 GPa also supports our observation. Also, the grain size reduction leading to progressive ultramylonite formation towards the core implies an increase in strain rate, where quartz and biotite behave as mechanically weaker compared to stiff magmatic alkali feldspars which align parallel to the shear zone [99, 100].

Further, lower amphibolite facies metamorphic assemblages in the eastern part of the shear zone (10 km north of Balehonnur) corresponding to cooling and exhumation indicate ca. 2400 Ma [29]. In contrast, in the northwest of the studied corridor, garnet and monazite from NW trending shear zones indicate ages of ca. 2500 ([101, 102]. Towards southeast garnet-bearing metamorphic assemblages along the southern margin of Bababudan basin and Holenarsipur greenstone belt indicate ca. 2520-2470 Ma [30]. These ages reveal the development of the regional shear zone network initiated by 2547-2520 Ma, which coincides with the lower crustal granulite facies event in the southern margin of the Western Dharwar craton [29].

Field-based tectonic fabrics data such as plastic strain in granite and absence of Koppa granite veins filled shears reveal that shear deformation initiated after 2610 Ma Koppa granite emplacement. Therefore, shear zone development post-dates the pluton emplacement, and Koppa granite corresponds to prekinematic pluton.

7.4. The Origin of Koppa Granite. The high contents of LIL (excluding ultramylonite) and HFS elements, including REE of the Koppa granite samples, preclude their derivation either through direct melting of mantle or from a mafic source. Melting of mafic crust originated at oceanic spreading centre (MORB) with strong depletion in incompatible elements [(0.16 wt.% K_2O, <2.88 ppm Rb and <29.2 ppm of Ba, $(La/Yb)_N = <0.84$; $Sr/Y = <3.5$ [103], cannot explain the observed high content of incompatible elements. Alternatively, the melting of preexisting TTGs (3350-3200 Ma; Jayananda et al. [32].) in the lower crustal levels can be considered. Melting of TTGs in the thickened lower crustal levels can generate potassic granites. Potassic granites of similar ages further east (Arsikere-Chitradurga-Pandavpura) have been attributed to the melting of TTGs in the lower crust (Jayananda et al. [24, 37]. However, the melting of lower crustal TTGs generates granite melts with higher SiO_2 contents and cannot explain the observed lower SiO_2 contents (56-69%). Globally, the diversity of Neoarchean granites is attributed to their origin from composite sources. Laurent et al. [13] have proposed a triangular discriminant plot of $3CaO\text{-}Al_2O_3/FeOt+MgO\text{-}5K_2O/Na_2O$ for granitoid sources where the Koppa granite samples plot on the high-K mafic source (Figure 10(a)). The observed high-K contents, together with the high content of incompatible elements, suggest composite sources either enriched lower crustal mafic rocks or melts originated from metasomatized upper mantle contaminated with lower crustal TTGs.

The following model is suggested for the heat source, melting conditions, and sources for Koppa granite. The emplacement of ca. 2610 Ma Koppa granites was immediately preceded by widespread ca. 2638 ± 66 Ma mafic volcanism in the adjoining Shimoga basin [104]. These magmas show depleted to the highly enriched character [89], and their interaction with the uppermost mantle and lower crust during their upward passage probably caused metasomatic enrichment in incompatible elements. Furthermore, their emplacement and eruption caused thermal blanketing and melting of enriched uppermost mantle and overlying lower crustal basement rocks, thus generating the granite magmas. The documented peak *P-T* conditions (775°C and 1.0-1.2 GPa) in the garnet-biotite rock in the Balehonnur shear zone are well within the range of melting of the lower part of the enriched mafic crust and consistent with the origin of granite magma. Alternatively, melts can be generated by enriched uppermost mantle and can be contaminated with lower crustal basement. The resultant granite magmas probably emplaced rapidly along with the contact between the TTG basement and greenstone as reflected in primary magmatic epidote.

The elemental and Nd isotope data of potassic granites in Chitradurga, Arsikere, and Pandavpura region emplaced during ca. 2620-2600 Ma originated by melting of preexisting lower crustal TTGs with minor mantle-derived juvenile input [34]. On the tectonic discriminant plots of Nb versus Y (Figure 10(b), after Pearce et al. [105]) and Nb/Y versus Nb+Y plot (Figure 10(c) after Whalen and Hilderbrand, [106]), the Koppa granite plot in the within plate A-type extending into Syn-collisional field. The Koppa granite and potassic plutons further NNW may be originated by melting of lower crustal TTG source during assembly of volcanic arc (Shimoga basin)–continent (3300-3150 Ma) TTG -3000-2800 Ma Bababudan-Western Ghat (greenstone belt).

7.5. Tectonic Significance of Balehonnur Shear Zone. The origin of crustal-scale shear zone patterns in Archean cratons has been interpreted by different thermo-mechanical and tectonic context [18, 19, 21, 107]. The cratonal strike-slip shear zones have been attributed to cratonic collisions [107], whereas Chardon et al. [18] argue that shear zone patterns in Archean craton are not due to amalgamation but linked to later crustal flow. Bouhallier [19] argued that the transcurrent shears result by a combination of relative vertical movements linked to body forces and crustal shortening linked to boundary forces.

Understanding the spatial relationship between granite emplacement and shear zone development is crucial as they place first-order constraints on the timing and duration of the orogenic system. The tectonic fabrics mapping in the Western Dharwar craton reveals widely spaced Neoarchean shear zone network [18]. Furthermore, strain fabrics analysis together with petrologic data, U-Pb zircon ages of potassic granites in the Western Dharwar suggest their emplacement coincided with second stage stabilization of Archean crust close to 2600 Ma followed by the development of widely spaced shear zones [18, 24]. These shear zones have been attributed to boundary forces and accommodated moderate shortening without large-scale displacements as documented along modern plate margin settings. Combined petrologic and geochronologic data on the metamorphic assemblages from major shear zones traversing WDC reveal the development of shear zones followed by regional metamorphism through slow cooling occurred during 2547-2400 Ma [29, 30, 98, 108]. Further north-west of Balehonnur shear zone, garnet-biotite schist from Kumata shear zone indicates *P-T* conditions 1.1 GPa and 790°C, and youngest zircon ages coincide with U-Pb monazite age of 2547 Ma probably correspond to the development of regional shear zones and metamorphism [108].

The crustal-scale Balehonnur shear zone traverses ca. 3300-3150 Ma TTG basement with ca. 3000 Ma old Western Ghat/Kudremukh greenstone belt [48, 109] (ca. 2900-2800 Ma old Bababudan greenstone belt [110], ca. 2630 Ma Shimoga greenstone belt [104], and 2610 Ma Koppa granite (this study). All the lithological assemblages affected by strong shear strain and kinematic analysis reveal a sinistral sense of displacement. Tectonic fabrics data and mineral reactions (feldspars totally consumed in the development of garnet) reveal that granite affected by plastic strain indicates shearing post-date the emplacement of potassic plutons.

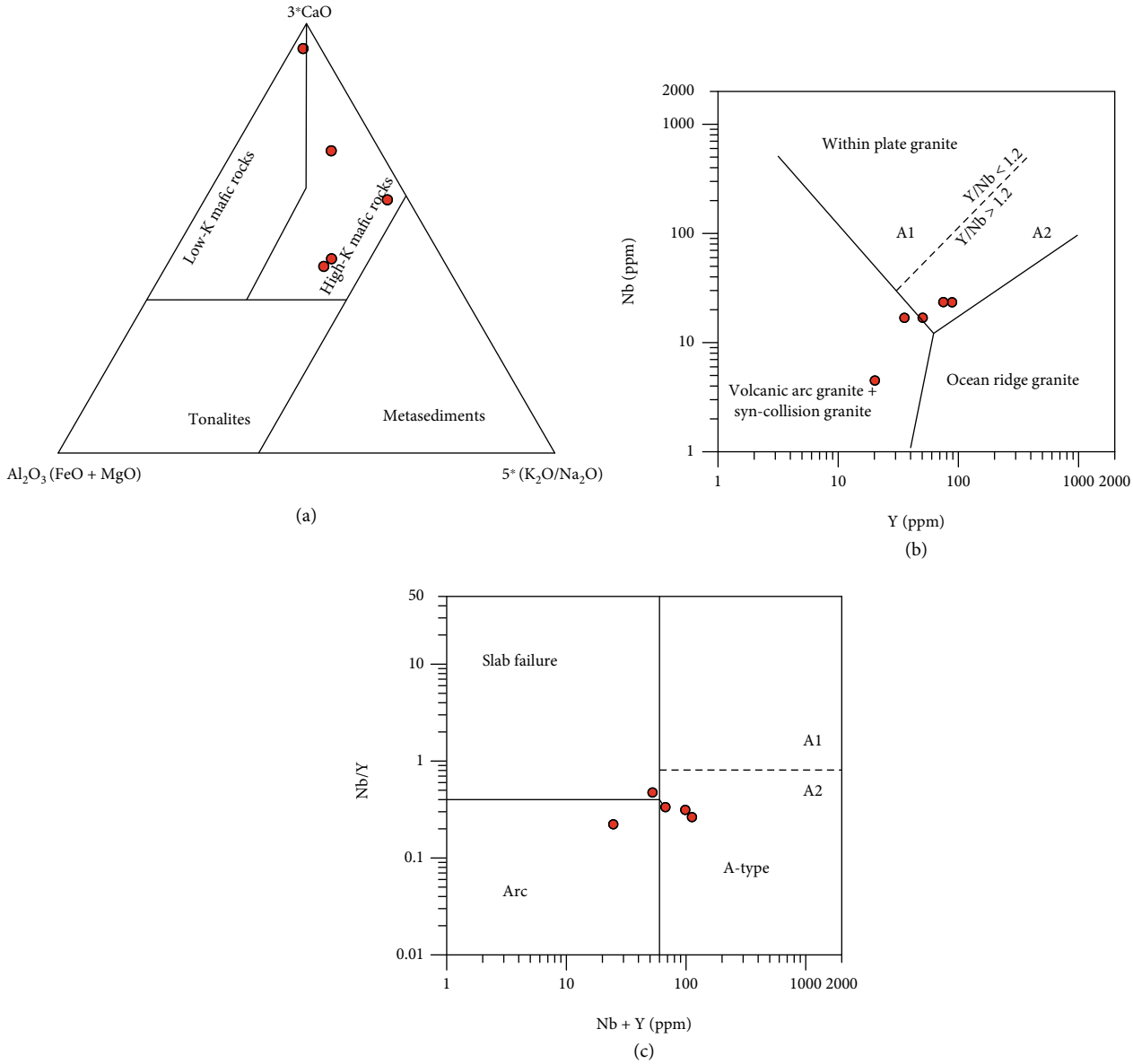

FIGURE 10: Source characterization and suggested tectonic setting. (a) In a 3CaO-Al_2O_3/FeOt+MgO-5K_2O/Na_2O plot, most samples plot in the tonalite field. (b, c) Nb versus Y (Pearce et al. [105]) plot and Nb/Y versus Nb+Y (Whalen and Hilderbrand [106]) plot showing the post-collisional A-type characteristics of current set of samples.

The thermo-mechanical processes of initiation of shear deformation and development of regional shear zone network are still debated [18, 20, 21]. The development of regional shear zones in the Western Dharwar craton is attributed to NE-SW shortening and sinistral transcurrent shearing in the foreland and arc-related, arc-normal, and arc-parallel displacements during Neoarchean oblique convergence [20]. On the other hand, Chardon et al. [18, 21] proposed that westward convergence of hot oceanic lithosphere during 2560-2500 Ma rejuvenated newly formed continental lithosphere in response to shortening by horizontal crustal flow against already cratonized older thickened continental crust (WDC). This tectonic movement leads to the development of strain heterogeneities between greenstone–TTGs/granites due to their different density and mechanical strength, eventually leading to the development of widely spaced shear zones along the boundary of greenstone belts without much horizontal displacement. The continued convergence of lithosphere and eventual assembly of crustal blocks causes regional shortening and strain portioning along major widely spaced shear zones in the WDC. Shear deformation, metamorphism, and fluid flow continued through the slow cooling of Archean crust until ca. 2400 Ma [30]. Such model accounts for the documented ca. 2600 Ma potassic plutonism, subsequent development of widely spaced crustal-scale shear zones, and final cratonization marking the end of the Archean Eon.

8. Conclusions

The development of crustal-scale sinistral Balehonnur shear zone initiated following the emplacement of ca. 2610 Ma Koppa granite, and shearing continued through peak metamorphism, followed by slow cooling ca. 2547-2450 Ma as documented further NNW in Kumata shear zone and Goa. The phase petrological and geochemical characteristics of the Koppa granite point towards the A-type geochemical character of the studied samples that probably originated by melting composite sources involving the uppermost enriched mantle and lower crustal basement. The zircon saturation temperature (Tzr = 1, 000°C) also implies magmatic emplacement temperature, higher than the general cut-off value, i.e., 830–850°C, for A-type granites [80]. Biotite stabilizes during post-emplacement water infiltration and cooling. Following biotite stabilization, the granite experienced shear deformation with an extremely high-strain rate leading to granite-mylonite formation. The sinistral shear imposes a metamorphic field gradient by stabilizing eclogite-high-pressure granulite facies garnet-biotite assemblages in the western and southern part of the shear zone.

In contrast, the mafic boudins in the eastern part experience low P-high T melting of amphibole, leading to stabilization of garnet. The contrasting *P-T* data from the western and eastern part of the shear zone imply shear zone development initiated probably during the amalgamation of the Bababudan greenstone belt with Shimoga and the Western Ghats belts, which in turn linked to the assembly of CDC with WDC, ca. 2560-2520 Ma.

Data Availability

Data tables are available as supplementary materials.

Conflicts of Interest

The authors declare that they have no conflicts of interest.

Acknowledgments

This work was partially funded by DST-FIST [SR/FST/ESI-146/2016(C)]. Tarun Kumar and Tarun Thomas supported by DST Inspire Fellowship. M. Guitreau and M. Jayananda acknowledges support from Region Auvergne, LabEx ClerVolc (ANR-10-LABX-0006), and the French Research Agency (project Zircontinents; ANR-17-CE31-0021). Aadhiseshan gratefully acknowledges the Dr. D.S. Kothari Post-doctoral Fellowship (DSKPDF). Balaji Rao supported by Shyama Prasad Mukherjee Fellowship (SPMF). Pritam NASIPURI acknowledges financial help from Personal Development Grant, IISER Bhopal for EPMA analysis. This is ClerVolc contribution 569.

Supplementary Materials

Supplementary 1. Appendix 1: (a) Phase topology of sample 18 MB-02 constructed using whole-rock bulk composition. (b) P-X (Composition) diagram showing the role of relative volumes of plagioclase and biotite in the garnet forming reaction. For a detailed discussion on the thermodynamic database and solution models used, readers may refer to *P-T* pseudosection subchapter.

Supplementary 2. Appendix 2: Major, trace, and rare-earth element content of the studied samples. The temperature (T_{zr}) estimated from Watson and Harrison [59] and Boenke et al. [60] is also appended against each sample.

Supplementary 3. Appendix 3: Zircon U-Pb data of the analyzed samples from the Balehonnur shear zone [113, 114].

Supplementary 4. Appendix 4: Details of the samples including GPS location, rock types, and mineral assemblages and ages.

References

[1] D. Chardon, O. Bamba, and K. Traoré, "Eburnean deformation pattern of Burkina Faso and the tectonic significance of shear zones in the West African craton," *BSGF - Earth Sciences Bulletin*, vol. 191, no. 1, p. 2, 2020.

[2] D. Chardon, P. Choukroune, and M. Jayananda, "Sinking of the Dharwar basin (South India): implications for Archaean tectonics," *Precambrian Research*, vol. 91, no. 1-2, pp. 15–39, 1998.

[3] J. H. Bédard, P. Brouillette, L. Madore, and A. Berclaz, "Archaean cratonization and deformation in the northern superior province, Canada: an evaluation of plate tectonic versus vertical tectonic models," *Precambrian Research*, vol. 127, no. 1-3, pp. 61–87, 2003.

[4] P. Choukroune, H. Bouhallier, and N. T. Arndt, "Soft lithosphere during periods of Archaean crustal growth or crustal reworking," *Geological Society, London, Special Publications*, vol. 95, no. 1, pp. 67–86, 1995.

[5] D. Chardon, P. Choukroune, and M. Jayananda, "Strain patterns, decollement and incipient sagducted greenstone terrains in the Archaean Dharwar craton (south India)," *Journal of Structural Geology*, vol. 18, no. 8, pp. 991–1004, 1996.

[6] W. J. Collins, M. J. Van Kranendonk, and C. Teyssier, "Partial convective overturn of Archaean crust in the east Pilbara craton, Western Australia: driving mechanisms and tectonic implications," *Journal of Structural Geology*, vol. 20, no. 9-10, pp. 1405–1424, 1998.

[7] M. J. Van Kranendonk, "Cool greenstone drips and the role of partial convective overturn in Barberton greenstone belt evolution," *Journal of the African Earth Sciences*, vol. 60, no. 5, pp. 346–352, 2011.

[8] P. Rey and G. Houseman, "Lithospheric scale gravitational flow: the impact of body forces on orogenic processes from Archaean to Phanerozoic," *Geological Society, London, Special Publications*, vol. 253, pp. 153–167, 2006.

[9] M. Brown, "Duality of thermal regimes is the distinctive characteristic of plate tectonics since the Neoarchean," *Geology*, vol. 34, no. 11, pp. 961–964, 2006.

[10] M. Brown, "Metamorphic conditions in orogenic belts: a record of secular change," *International Geology Review*, vol. 49, no. 3, pp. 193–234, 2007.

[11] M. Brown, "Metamorphism, plate tectonics, and the supercontinent cycle," *Earth Science Frontiers*, vol. 14, no. 1, pp. 1–18, 2007.

[12] T. Gerya, "Precambrian geodynamics: concepts and models," *Gondwana Research*, vol. 25, no. 2, pp. 442–463, 2014.

[13] O. Laurent, H. Martin, J. F. Moyen, and R. Doucelance, "The diversity and evolution of late-Archean granitoids: evidence for the onset of "modern-style" plate tectonics between 3.0 and 2.5 Ga," *Lithos*, vol. 205, pp. 208–235, 2014.

[14] P. Rey and N. Coltice, "Neoarchean lithospheric strengthening and the coupling of Earth's geochemical reservoirs," *Geology*, vol. 36, no. 8, p. 635, 2008.

[15] F. Clos, I. Zibra, and R. Weinberg, *Building the Archean Continental Crust: 300 ma of Felsic Magmatism in the Yalgoo Dome (Yilgarn Craton)*, Geological Survey of Western Australia, Perth, Australia, 2018.

[16] G. Beakhouse, "Structurally controlled, magmatic hydrothermal model for Archean lode gold deposits: a working hypothesis," *Ontario Geological Survey, Open File Report*, vol. 6193, p. 133, 2007.

[17] J. Kolb, A. Hellmann, A. Rogers et al., "The role of a transcrustal shear zone in orogenic gold mineralization at the Ajjanahalli mine, Dharwar craton, South India," *Economic Geology*, vol. 99, no. 4, pp. 743–759, 2004.

[18] D. Chardon, M. Jayananda, T. R. Chetty, and J. J. Peucat, "Precambrian continental strain and shear zone patterns: South Indian case," *Journal of Geophysical Research - Solid Earth*, vol. 113, no. B8, p. 8402, 2008.

[19] H. Bouhallier, P. Choukroune, and M. Ballèvre, "Diapirism, bulk homogeneous shortening and transcurrent shearing in the Archaean Dharwar craton: the Holenarsipur area, southern India," *Precambrian Research*, vol. 63, no. 1-2, pp. 43–58, 1993.

[20] B. Chadwick, V. N. Vasudev, and G. V. Hegde, "The Dharwar craton, southern India, interpreted as the result of late Archaean oblique convergence," *Precambrian Research*, vol. 99, no. 1-2, pp. 91–111, 2000.

[21] D. Chardon, M. Jayananda, and J.-J. J. Peucat, "Lateral constrictional flow of hot orogenic crust: Insights from the Neoarchean of south India, geological and geophysical implications for orogenic plateaux," *Geochemistry, Geophysics, Geosystems*, vol. 12, no. 2, 2011.

[22] V. V. Rao, A. S. Murty, D. Sarkar et al., "Crustal velocity structure of the Neoarchean convergence zone between the eastern and western blocks of Dharwar craton, India from seismic wide-angle studies," *Precambrian Research*, vol. 266, pp. 282–295, 2015.

[23] M. Jayananda, M. Santosh, and K. R. Aadhiseshan, "Formation of Archean (3600-2500 Ma) continental crust in the Dharwar Craton, southern India," *Earth-Science Reviews*, vol. 181, pp. 12–42, 2018.

[24] M. Jayananda, D. Chardon, J.-J. Peucat, and R. Capdevila, "2.61 Ga potassic granites and crustal reworking in the western Dharwar craton, southern India: tectonic, geochronologic and geochemical constraints," *Precambrian Research*, vol. 150, no. 1-2, pp. 1–26, 2006.

[25] M. Jayananda, G. Martin, T. T. Thomas et al., "Geochronology and geochemistry of Meso- to Neoarchean magmatic epidote-bearing potassic granites, Western Dharwar Craton (Bellur–Nagamangala–Pandavpura corridor), Southern India: implications for the successive stages of crustal reworking and cratonization," *Geological Society, London, Special Publications*, vol. 489, pp. 79–114, 2020.

[26] F. Corfu and V. S. Hegde, "U-Pb systematics of the western Dharwar Craton-glimpses of a billion year history of crustal evolution and relations to ancient supercratons," *Journal of South American Earth Sciences*, vol. 102, article 102659, 2020.

[27] W. Ao, M. Zhai, Y. Zhao et al., "Paleo-Mesoarchean crustal growth and reworking in the western Dharwar craton, southwestern India: evidence from trondhjemitic gneiss and granitic gneiss," *Precambrian Research*, vol. 367, article 106428, 2021.

[28] M. N. Ramakrishnan, M. Viswanatha, and J. Swami Nath, "Basement-cover relationships of Peninsular Gneisses with high grade schists and greenstone belts of southern Karnataka," *Journal of the Geological Society of India*, vol. 17, pp. 97–117, 1976.

[29] J.-J. Peucat, M. Jayananda, D. Chardon, R. Capdevila, C. M. Fanning, and J.-L. Paquette, "The lower crust of the Dharwar craton, southern India: patchwork of Archean granulitic domains," *Precambrian Research*, vol. 227, pp. 4–28, 2013.

[30] M. Jayananda, J. J. Peucat, D. Chardon, B. K. Rao, C. M. Fanning, and F. Corfu, "Neoarchean greenstone volcanism and continental growth, Dharwar craton, southern India: constraints from SIMS U-Pb zircon geochronology and Nd isotopes," *Precambrian Research*, vol. 227, pp. 55–76, 2013.

[31] M. Guitreau, S. B. Mukasa, L. Loudin, and S. Krishnan, "New constraints on the early formation of the Western Dharwar craton (India) from igneous zircon U-Pb and Lu-Hf isotopes," *Precambrian Research*, vol. 302, pp. 33–49, 2017.

[32] M. Jayananda, D. Chardon, J. Peucat, and C. M. Fanning, "Paleo- to Mesoarchean TTG accretion and continental growth in the western Dharwar craton, Southern India: constraints from SHRIMP U–Pb zircon geochronology, whole-rock geochemistry and Nd–Sr isotopes," *Precambrian Research*, vol. 268, pp. 295–322, 2015.

[33] A. Dasgupta, S. K. Bhowmik, S. Dasgupta, J. Avila, and T. R. Ireland, "Mesoarchaean clockwise metamorphic P-T path from the Western Dharwar craton," *Lithos*, vol. 342-343, pp. 370–390, 2019.

[34] M. Jayananda, M. Santosh, and B. M. Jahn, "Precambrian accretionary orogens," *Precambrian Research*, vol. 227, pp. 1–3, 2013.

[35] M. J. D. M. Banerjee, N. C. Pant, S. Dasgupta, T. Kano, N. Mahesha, and B. Mahableswar, "2.62 Ga high-temperature metamorphism in the central part of the eastern Dharwar craton: implications for late Archaean tectonothermal history," *Geological Journal*, vol. 47, no. 2–3, pp. 213–236, 2012.

[36] X. Wang, X. P. Li, J. Zhang, and H. P. Schertl, "Geochemistry, geochronology and evolution of Paleoproterozoic granitoid gneisses in the Khondalite Belt, North China craton," *Precambrian Research*, vol. 338, article 105590, 2020.

[37] M. Jayananda, K. R. Aadhiseshan, M. A. Kuiak et al., "Multi-stage crustal growth and Neoarchean geodynamics in the eastern Dharwar craton, southern India," *Gondwana Research*, vol. 78, pp. 228–260, 2020.

[38] R. Srinivasan and R. W. Ojakangas, "Sedimentology of quartz-pebble conglomerates and quartzites of the Archean Bababudan group, Dharwar craton, South India: evidence for early crustal stability," *Journal of Geology*, vol. 94, no. 2, pp. 199–214, 1986.

[39] B. P. Chadwick, M. Ramakrishnan, and M. N. Viswanatha, "Bababudan-a late Archaean intracratonic volcanosedimentary basin, Karnataka, southern India. Part II: structure," *Journal of the Geological Society of India*, vol. 26, pp. 802–821, 1985.

[40] B. Chadwick, M. Ramakrishnan, V. N. Vasudev, and M. N. Viswanatha, "Facies distributions and structure of a Dharwar volcanosedimentary basin: evidence for late Archaean transpression in southern India?," *Journal of the Geological Society of London*, vol. 146, no. 5, pp. 825–834, 1989.

[41] B. P. Chadwick, M. Ramakrishnan, and M. N. Viswanatha, "Structural and metamorphic relations between Sargur and Dharwar supracrustal rocks and peninsular gneiss in Central Karnataka," *Journal of the Geological Society of India*, vol. 22, pp. 557–569, 1981.

[42] A. P. Nutman, B. Chadwick, B. Krishna Rao, and V. N. Vasudev, "SHRIMP U/Pb zircon ages of acid volcanic rocks in the Chitradurga and Sandur groups, and granites adjacent to the Sandur schist belt, Karnataka," *Journal of the Geological Society of India*, vol. 47, pp. 153–164, 1996.

[43] M. R. Mohan, D. S. Sarma, N. J. Mc Naughton et al., "SHRIMP zircon and titanite U-Pb ages, Lu-Hf isotope signatures and geochemical constraints for ~2.56 Ga granitic magmatism in Western Dharwar craton, Southern India: evidence for short-lived Neoarchean episodic crustal growth?," *Precambrian Research*, vol. 243, pp. 197–220, 2014.

[44] D. Chardon and M. Jayananda, "Three-dimensional field perspective on deformation, flow, and growth of the lower continental crust (Dharwar craton, India)," *Tectonics*, vol. 27, no. 1, 2008.

[45] S. A. Drury and R. W. Holt, "The tectonic framework of the south Indian craton: a reconnaissance involving LANDSAT imagery," *Tectonophysics*, vol. 65, no. 3-4, pp. T1–T15, 1980.

[46] T. R. K. Chetty, D. P. Mohanty, and T. Yellappa, "Mapping of shear zones in the Western Ghats, southwestern part of Dharwar craton," *Journal of the Geological Society of India*, vol. 79, no. 2, pp. 151–154, 2012.

[47] M. Brown, "Characteristic thermal regimes of plate tectonics and their metamorphic imprint throughout E arth history: when did Earth first adopt a plate tectonics mode of behavior," *Geological Society of America Special Papers*, vol. 440, pp. 97–128, 2008.

[48] S. A. Drury, N. B. W. Harris, R. W. Holt, G. J. Reeves-Smith, and R. T. Wightman, "Precambrian tectonics and crustal evolution in south India," *Journal of Geology*, vol. 92, no. 1, pp. 3–20, 1984.

[49] M. Ramakrishnan and R. Vaidyanadhan, "Geology of India," *Geological Society of India*, vol. v1, p. 556, 2008.

[50] R. Das and S. S. Rai, "Redefining Dharwar Craton-Southern granulite terrain boundary in south India from new seismological constraints," *Precambrian Research*, vol. 332, article 105394, 2019.

[51] A. K. Krishna, T. C. Khanna, and K. R. Mohan, "Rapid quantitative determination of major and trace elements in silicate rocks and soils employing fused glass discs using wavelength dispersive X-ray fluorescence spectrometry," *Spectrochimica Acta Part B: Atomic Spectroscopy*, vol. 122, pp. 165–171, 2016.

[52] M. Satyanarayanan, V. Balaram, S. S. Sawan et al., "Rapid determination of REEs, PGEs, and other trace elements in geological and environmental materials by high resolution inductively coupled plasma mass spectrometry," *Atomic Spectroscopy*, vol. 39, no. 1, pp. 1–15, 2018.

[53] M. Guitreau, A. Gannoun, Z. Deng et al., "Stable isotope geochemistry of silicon in granitoid zircon," *Geochimica et Cosmochimica Acta*, vol. 316, pp. 273–294, 2022.

[54] M. Wiedenbeck and J. N. Goswami, "High precision 207Pb206Pb zircon geochronology using a small ion microprobe," *Geochimica et Cosmochimica Acta*, vol. 58, no. 9, pp. 2135–2141, 1994.

[55] J. B. Paces and J. D. Miller, "Precise U-Pb ages of Duluth complex and related mafic intrusions, northeastern Minnesota' geochronological insights to physical, petrogenetic, paleomagnetic, and tectonomagmatic processes associated with the 1.1 Ga midcontinent rift system," *Journal of Geophysical Research - Solid Earth*, vol. 98, no. 93, pp. 13997–14013, 1993.

[56] J. Slama, J. Kosler, D. J. Condon et al., "Plešovice zircon—a new natural reference material for U-Pb and Hf isotopic microanalysis," *Chemical Geology*, vol. 249, no. 1-2, pp. 1–35, 2008.

[57] D. L. Whitney and B. W. Evans, "Abbreviations for names of rock-forming minerals," *American Mineralogist*, vol. 95, no. 1, pp. 185–187, 2010.

[58] T. D. Hoisch, "Empirical calibration of six geobarometers for the mineral assemblage quartz+muscovite+biotite+plagioclase+garnet," *Contributions to Mineralogy and Petrology*, vol. 104, no. 2, pp. 225–234, 1990.

[59] E. B. Watson and T. M. Harrison, "Zircon saturation revisited' temperature and composition effects in a variety of crustal magma types," *Earth and Planetary Science Letters*, vol. 64, no. 2, pp. 295–304, 1983.

[60] P. Boehnke, E. B. Watson, D. Trail, T. M. Harrison, and A. K. Schmitt, "Zircon saturation re-revisited," *Chemical Geology*, vol. 351, pp. 324–334, 2013.

[61] J. A. D. Connolly, "The geodynamic equation of state: what and how," *Geochemistry, Geophysics, Geosystems*, vol. 10, pp. 1–19, 2009.

[62] T. J. B. Holland and R. Powell, "An improved and extended internally consistent thermodynamic dataset for phases of petrological interest, involving a new equation of state for solids," *Journal of Metamorphic Geology*, vol. 29, no. 3, pp. 333–383, 2011.

[63] R. W. White, R. Powell, and T. J. B. Holland, "Progress relating to calculation of partial melting equilibria for metapelites," *Journal of Metamorphic Geology*, vol. 25, no. 5, pp. 511–527, 2007.

[64] L. Tajcmanova, J. Connolly, and B. Cesare, "A thermodynamic model for titanium and ferric iron solution in biotite," *Journal of Metamorphic Geology*, vol. 27, no. 2, pp. 153–165, 2009.

[65] R. C. Newton, T. V. Charlu, and O. J. Kleppa, "Thermochemistry of the high structural state plagioclases," *Geochimica et Cosmochimica Acta*, vol. 44, no. 7, pp. 933–941, 1980.

[66] T. J. B. Holland and R. Powell, "An internally consistent thermodynamic data set for phases of petrological interest," *Journal of Metamorphic Geology*, vol. 16, no. 3, pp. 309–343, 1998.

[67] T. J. B. Holland and R. Powell, "Calculation of phase relations involving haplogranitic melts using an internally consistent thermodynamic dataset," *Journal of Petrology*, vol. 42, no. 4, pp. 673–683, 2001.

[68] W. A. Deer, R. A. Howie, and J. Zussman, *An introduction to the rock-forming minerals*, Mineralogical Society of Great Britain and Ireland, 2013.

[69] E. C. R. R. Green, R. W. White, J. F. A. A. Diener, R. Powell, T. J. B. Holland, and R. M. Palin, "Activity–composition relations for the calculation of partial melting equilibria in

metabasic rocks," *Journal of Metamorphic Geology*, vol. 34, no. 9, pp. 845–869, 2016.

[70] T. J. B. Holland, E. C. R. Green, and R. Powell, "Melting of peridotites through to granites: a simple thermodynamic model in the system KNCFMASHTOCr," *Journal of Petrology*, vol. 59, no. 5, pp. 881–900, 2018.

[71] P. Nasipuri, A. Bhattacharya, and S. Das, "Metamorphic reactions in dry and aluminous granulites: a Perple_X P-T pseudosection analysis of the influence of effective reaction volume," *Contributions to Mineralogy and Petrology*, vol. 157, no. 3, pp. 301–311, 2009.

[72] X. M. Yang, "Estimation of crystallization pressure of granite intrusions," *Lithos*, vol. 286-287, pp. 324–329, 2017.

[73] E. Achterbergh, C. Ryan, and W. Griffin, *GLITTER: On-Line Interactive Data Reduction for the Laser Ablation ICP-MS Microprobe*, Ninth Annual V. M. Goldschmidt Conference, Cambridge, 2000.

[74] K. R. Ludwig, *Isoplot A geochronological tool kit for Microsoft Excell*, 4Berkeley Geochronol Cent Spec Publ, 2009.

[75] N. Sorcar, K. B. Joshi, E. P. Oliveira, J. K. Tomson, and V. Nandakumar, "Characterization of partial melting events in garnet-cordierite gneiss from the Kerala Khondalite Belt, India," *Geoscience Frontiers*, vol. 11, no. 2, pp. 597–611, 2020.

[76] B. Cesare, S. Ferrero, E. Salvioli-Mariani, D. Pedron, and A. Cavallo, "'Nanogranite' and glassy inclusions: the anatectic melt in migmatites and granulites," *Geology*, vol. 37, no. 7, pp. 627–630, 2009.

[77] E. W. Sawyer, "Criteria for the recognition of partial melting," *Physics and Chemistry of the Earth, Part A: Solid Earth and Geodesy*, vol. 24, no. 3, pp. 269–279, 1999.

[78] L. Menegon, P. Nasipuri, H. Stünitz, H. Behrens, and E. Ravna, "Dry and strong quartz during deformation of the lower crust in the presence of melt," *Journal of Geophysical Research - Solid Earth*, vol. 116, no. B10, 2011.

[79] J. D. Clemens and D. Vielzeuf, "Constraints on melting and magma production in the crust," *Earth and Planetary Science Letters*, vol. 86, no. 2-4, pp. 287–306, 1987.

[80] J. D. Clemens, J. R. Holloway, and A. J. R. White, "Origin of an A-type granite; experimental constraints," *American Mineralogist*, vol. 71, no. 324, p. 317, 1986.

[81] M. J. Holdaway, B. Mukhopadhyay, M. D. Dyar, C. V. Guidotti, and B. L. Dutrow, "Garnet-biotite geothermometry revised: new Margules parameters and a natural specimen data set from Maine," *American Mineralogist*, vol. 82, no. 5-6, pp. 582–595, 1997.

[82] M. J. Holdaway, "Application of new experimental and garnet Margules data to the garnet-biotite geothermometer," *American Mineralogist*, vol. 85, no. 7-8, pp. 881–892, 2000.

[83] R. M. Palin, O. M. Weller, D. J. Waters, and B. Dyck, "Quantifying geological uncertainty in metamorphic phase equilibria modelling; a Monte Carlo assessment and implications for tectonic interpretations," *Geoscience Frontiers*, vol. 7, no. 4, pp. 591–607, 2016.

[84] D. Hernández-Uribe and R. Palin, "A revised petrological model for subducted oceanic crust: insights from phase equilibrium modelling," *Journal of Metamorphic Geology*, vol. 37, no. 6, pp. 745–768, 2019.

[85] T. Holland and J. Blundy, "Non-ideal interactions in calcic amphiboles and their bearing on amphibole-plagioclase thermometry," *Contributions to Mineralogy and Petrology*, vol. 116, no. 4, pp. 433–447, 1994.

[86] S. Bhadra and A. Bhattacharya, "The barometer tremolite + tschermakite + 2 albite = 2 pargasite + 8 quartz: constraints from experimental data at unit silica activity, with application to garnet-free natural assemblages," *American Mineralogist*, vol. 92, no. 4, pp. 491–502, 2007.

[87] L. Tajčmanová, J. Konopásek, and J. A. D. Connolly, "Diffusion-controlled development of silica-undersaturated domains in felsic granulites of the bohemian massif (Variscan belt of Central Europe)," *Contributions to Mineralogy and Petrology*, vol. 153, no. 2, pp. 237–250, 2007.

[88] V. Gardien, A. B. Thompson, D. Grujic, and P. Ulmer, "Experimental melting of biotite + plagioclase + quartz ± muscovite assemblages and implications for crustal melting," *Journal of Geophysical Research*, vol. 100, no. B8, pp. 15581–15591, 1995.

[89] J. L. Vigneresse, P. Barbey, and M. Cuney, "Rheological transitions during partial melting and crystallization with application to felsic magma segregation and transfer," *Journal of Petrology*, vol. 37, pp. 1579–1600, 1996.

[90] R. C. Newton, J. R. Ashworth, and M. Brown, "Fluids and melting in the Archaean deep crust of south India," *High-temperature metamorphism and crustal anatexis*, pp. 149 - 179, 1990.

[91] J. B. Whalen, K. L. Currie, and B. W. Chappell, "A-type granites: geochemical characteristics, discrimination and petrogenesis," *Contributions to Mineralogy and Petrology*, vol. 95, no. 4, pp. 407–419, 1987.

[92] M. Guitreau and J. Flahaut, "Record of low-temperature aqueous alteration of Martian zircon during the late Amazonian," *Nature Communications*, vol. 10, no. 1, p. 2457, 2019.

[93] D. Rubatto, "Zircon trace element geochemistry: partitioning with garnet and the link between U-Pb ages and metamorphism," *Chemical Geology*, vol. 184, no. 1-2, pp. 123–138, 2002.

[94] N. Le Breton and A. B. Thompson, "Fluid-absent (dehydration) melting of biotite in metapelites in the early stages of crustal anatexis," *Contributions to Mineralogy and Petrology*, vol. 99, no. 2, pp. 226–237, 1988.

[95] A. E. Patino Douce and J. S. Beard, "Dehydration-melting of biotite gneiss and quartz amphibolite from 3 to 15 kbar," *Journal of Petrology*, vol. 36, no. 3, pp. 707–738, 1995.

[96] A. Zeh, T. J. B. Holland, and R. Klemd, "Phase relationships in grunerite–garnet-bearing amphibolites in the system CFMASH, with applications to metamorphic rocks from the central zone of the Limpopo Belt, South Africa," *Journal of Metamorphic Geology*, vol. 23, no. 1, pp. 1–17, 2005.

[97] R. F. Weinberg, A. N. Sial, and G. Mariano, "Close spatial relationship between plutons and shear zones," *Geology*, vol. 32, no. 5, pp. 377–380, 2004.

[98] S. Rekha, A. Bhattacharya, and T. A. Viswanath, "Microporosity linked fluid focusing and monazite instability in greenschist facies para-conglomerates, western India," *Geochimica et Cosmochimica Acta*, vol. 105, pp. 187–205, 2013.

[99] R. Vernon, "A practical guide to rock microstructure," Cambridge University Press, 2004.

[100] C. H. Scholz, S. Edi, and G. Schubert, "6.10- fault mechanics*Treatise on Geophysics*, , 433 - 468, 2007), .

[101] S. Rekha and A. Bhattacharya, "Growth, preservation of Paleoproterozoic-shear-zone-hosted monazite, north of the Western Dharwar craton (India), and implications for Gondwanaland assembly," *Contributions to Mineralogy and Petrology*, vol. 166, no. 4, pp. 1203–1222, 2013.

[102] S. Rekha, A. Bhattacharya, and N. Chatterjee, "Tectonic restoration of the Precambrian crystalline rocks along the west coast of India: correlation with eastern Madagascar in East Gondwana," *Precambrian Research*, vol. 252, pp. 191–208, 2014.

[103] A. Gale, C. A. Dalton, C. H. Langmuir, Y. Su, and J.-G. Schilling, "The mean composition of ocean ridge basalts," *Geochemistry, Geophysics, Geosystems*, vol. 14, no. 3, pp. 489–518, 2013.

[104] A. Giri, R. Anand, S. Balakrishnan, J. K. Dash, and D. S. Sarma, "Neoarchean magmatism in Shimoga greenstone belt, India: evidence for subduction-accretion processes in the evolution of the western Dharwar stratigraphy," *Lithos*, vol. 330-331, pp. 177–193, 2019.

[105] J. A. Pearce, N. B. W. Harris, and A. Tindle, "Trace element discrimination diagrams for the tectonic interpretation of granitic rocks," *Journal of Petrology*, vol. 25, no. 4, pp. 956–983, 1984.

[106] J. Whalen and R. Hildebrand, "Trace element discrimination of arc, slab failure, and A-type granitic rocks," *Lithos*, vol. 348-349, article 105179, 2019.

[107] P. J. Treloar, M. P. Coward, and N. B. W. Harris, "Himalayan-Tibetan analogies for the evolution of the Zimbabwe craton and Limpopo Belt," *Precambrian Research*, vol. 55, no. 1-4, pp. 571–587, 1992.

[108] C. Ishwar-Kumar, M. Santosh, S. A. Wilde et al., "Mesoproterozoic suturing of Archean crustal blocks in western peninsular India: implications for India–Madagascar correlations," *Lithos*, vol. 263, pp. 143–160, 2016.

[109] R. Kerrich and A. Polat, "Archean greenstone-tonalite duality: thermochemical mantle convection models or plate tectonics in the early earth global dynamics?," *Tectonophysics*, vol. 415, no. 1-4, pp. 141–165, 2006.

[110] A. Kumar, Y. J. B. Rao, T. V. Sivaraman, and K. Gopalan, "Sm-Nd ages of Archaean metavolcanics of the Dharwar craton, South India," *Precambrian Research*, vol. 80, no. 3-4, pp. 205–216, 1996.

[111] J. T. O'Connor, *A classification of quartz-rich igneous rocks based on feldspar ratios*, 525U.S. Geological Survey, 1965.

[112] F. Barker, "Trondhjemite: definition, environment and hypotheses of origin," in *Trondhjemites, Dacites and Related Rocks*, F. Barker, Ed., pp. 1–12, Elsevier, Amsterdam, Netherlands, 1979.

[113] A. Gerdes and A. Zeh, "Combined U-Pb and Hf isotope LA-(MC-)ICP-MS analyses of detrital zircons: comparison with SHRIMP and new constraints for the provenance and age of an Armorican metasediment in Central Germany," *Earth and Planetary Science Letters*, vol. 249, no. 1-2, pp. 47–61, 2006.

[114] M. Guitreau and J. Blichert-Toft, "Implications of discordant U-Pb ages on Hf isotope studies of detrital zircons," *Chemical Geology*, vol. 385, pp. 17–25, 2014.